1   **Revision 2: The origin of Ti-oxide minerals below and within the eastern Athabasca Basin,**

2   **Canada**

3   Erin E. Adlakha[1,2], Keiko Hattori[2], Mitchell J. Kerr[1] and Brandon M. Boucher[3]

4   [1]Department of Geology, Saint Mary's University, 923 Robie St., Halifax, Nova Scotia, Canada,

5   B3H3C3

6   [2]Department of Earth and Environmental Sciences, University of Ottawa, 25 Templeton Dr.,

7   Ottawa, Ontario, Canada, K1N6N5

8   [3]Department of Earth Sciences, University of New Brunswick, 2 Bailey Drive, Fredericton, New

9   Brunswick, Canada, E3B5A3

10   Corresponding author: erin.adlakha@smu.ca

11   **Abstract**

12   Titanium oxide minerals along the P2 fault in the eastern Athabasca Basin are characterized to

13   constrain their origin and the geological history of the area. Two types of rutile are recognized in

14   the basement rocks. Early rutile is disseminated in graphitic metapelite and quartzite and formed

15   during regional metamorphism and post-metamorphic hydrothermal activity. Late rutile occurs

16   as a needle-like alteration product of mica and likely formed during retrogression of the

17   basement. In graphitic metapelite, early rutile commonly occurs with an assemblage of oxy-

18   dravite, quartz, graphite, zircon, pyrite, biotite and muscovite. In quartzite, rutile occurs with

19   quartz, sillimanite, and zircon. Metamorphic rutile is characterized by high Nb/Ta ratios (up to

20   47) with high concentrations of U (up to 126 ppm) and V^{4+} (up to 1.44 wt%; V valance

21   calculated from EPMA data). Hydrothermal rutile contains distinctly low Nb/Ta (as low as 4.80)

22   with high Ta (≤3050 ppm), and relatively low V (as V^{3+}; as low as 0.02 wt.%) and U (as low as

23   9.06 ppm), reflecting fluids in reduced oxidation conditions. Anatase forms small anhedral

24   (rarely coarse and euhedral) grains in the basal sandstones and altered basement rocks. In

25   sandstones, anatase occurs with the late diagenetic mineral assemblage, whereas in basement

26   rocks it commonly occurs with the clay-sized minerals related to uranium mineralization. In both

27   rocks, anatase likely formed through the dissolution of rutile and/or other Ti-bearing minerals.

28   Anatase is characterized by variably high Fe (up to 0.99 wt.%; possibly contributed by hematite

29   micro- or nanoinclusions) and U (up to 180 ppm). The mineral assemblages and composition of

30   anatase suggest its protracted crystallization from relatively low temperature, oxidizing, acidic,

31   uraniferous fluids from the sandstones during late diagenesis and hydrothermal activity.

32   Therefore, the occurrence of anatase records the incursion of basin fluids into the basement, and

33   the interaction of basement rocks with fluids responsible for the formation of the McArthur River

34   uranium deposit. The results of this study confirm that Ti-oxides are useful in unraveling the

35   geological history of an area that underwent prolonged hydrothermal activity.

36   Keywords: rutile, anatase, P2 fault, McArthur River, unconformity-type uranium deposits,

37   alteration

Introduction

39   The Paleoproterozoic Athabasca Basin, and crystalline basement rocks, experienced

40   multiple alteration events including the hydrothermal activity related to the formation of world-

41   class unconformity-type uranium deposits. Many petrological studies over the past 40 years aim

42   to unravel the paragenesis of the area (e.g., Hoeve and Sibbald 1977; Kotzer and Kyser 1995;

43   Fayek and Kyser 1997; Alexandre et al. 2005, 2009, 2012; Cloutier et al. 2011; Reid et al. 2014;

2

44   Adlakha and Hattori 2015, 2016), in order to evaluate the nature of uranium mineralization and

45   its timing with respect to the geological evolution of the area. This information is critical to

46   assess the conditions and geological environments for the formation of these giant uranium

47   deposits. Although Ti-oxide minerals are noted in these rocks (e.g., Kotzer and Kyser 1995;

48   Fayek and Kyser 1997; Alexandre et al. 2005, 2009; Cloutier et al. 2009, 2010, 2011), there have

49   been no detailed studies of the minerals.

50   Titanium-oxide minerals form different polymorphs (rutile, anatase, brookite) and

51   accommodate a wide variety of minor elements, reflecting their crystallizing environments (e.g.,

52   Meinhold 2010). Although the P-T conditions for the polymorph's stability are not well

53   constrained, considering contradicting interpretations (Osborn, 1953; Dachille et al., 1968, 1969;

54   Jameison and Olinger, 1969; Gribb and Banfield 1997; Zhang and Banfield 1999, 2000; Ranade

55   et al. 2002; Navrotsky 2003; Levchenko et al. 2006; Smith et al. 2009; Mei et al. 2014; Curnan

56   and Kitchin 2015, Plavsa et al. 2018), it is generally accepted that rutile is more stable than

57   anatase, and the polymorphic transition of anatase to rutile is favourable over rutile to anatase

58   under most conditions (Dachille et al. 1968). This is supported by observations of rutile in both

59   high and low temperature environments, and anatase in only low temperature environments.

60   Regardless of the polymorph stability, it is apparent that rutile is the most common Ti-oxide

61   polymorph in Earth's crust (Meinhold et al. 2010). It occurs in metamorphic rocks of various

62   facies ranging from greenschist to granulite and eclogite; as detrital and authigenic grains in

63   sedimentary rocks; in igneous rocks, particularly evolved granitic rocks and pegmatite (Černý

64   1989); and in hydrothermally altered rocks and metallic mineral deposits including Cu-Mo

65   porphyry deposits, volcanogenic massive sulphide deposits and orogenic Au deposits (e.g.,

66   Schandl et al. 1990; Urban et al. 1992; Scott 2005; Scott and Radford 2007; Rabbia et al. 2009;

3

67   Agangi et al. 2019). Once rutile is crystallized, it is usually resistant to hydrothermal alteration

68   owing to the insoluble nature of Ti in most aqueous fluids (e.g., Ayers and Watson 1993).

69   Anatase is indicative of low temperature, aqueous environments, such as diagenetic systems

70   (Smith et al. 2009), along with less common brookite. Anatase is commonly reported as an

71   authigenic mineral in siliciclastic sedimentary rocks (e.g., Morad and Aldahan 1986; Morad

72   1986; Pe-Piper et al. 2011), and likely forms through the breakdown of detrital titaniferous

73   minerals, such as Ti-rich oxides, biotite, and titanite. Considering these properties, Ti-oxide

74   minerals may be useful in petrologic studies of altered rocks, such as those common in the

75   Athabasca Basin.

76   This paper describes the occurrence, polymorphs, and chemical composition of Ti-oxide

77   in well-characterized samples of metasedimentary basement and Athabasca sandstone along the

78   P2 fault, which is the major structure in the eastern basin and hosts all ore bodies of the

79   exceptionally high-grade McArthur River uranium deposit (Fig. 1). The P2 fault is not only an

80   important structural control for mineralization, but also served as a fluid pathway during

81   uriniferous hydrothermal activity (Adlakha and Hattori 2015, 2016; Adlakha et al. 2017). The

82   study integrates micro-analytical data using a field emission scanning electron microscope

83   (SEM) for detailed textural analysis, Raman spectroscopy to identify Ti-oxide polymorphs,

84   electron probe microanalysis (EPMA) to quantify major element abundances, and laser ablation

85   inductively coupled plasma mass spectroscopy (LA-ICP-MS) for trace element abundances. The

86   data are used to evaluate the origin and relative timing of Ti-oxide crystallization. This

87   information is used to constrain the paragenetic history of this economically important area.

4

Geological Background

88

Regional Geology

89

90   The basement below the eastern Athabasca Basin belongs to the Wollaston supergroup,

91 which consists of Paleoproterozoic metasedimentary rocks, including metapelite, graphitic

92 metapelite, meta-arkose, calc-silicate, and quartzite, intruded by anatexic granitic lenses (Fig. 1).

93 Regional metamorphism of the Wollaston supergroup during the 1.92 to 1.80 Ga Trans-Hudson

94 Orogen reached upper amphibolite to lower granulite facies conditions (Annesley et al. 2005;

95 Corrigan et al. 2009). The origin of quartzite, which forms topographic highs at the

96 unconformity, is debated. The rocks are considered to have formed during regional

97 metamorphism of quartz-rich sedimentary rocks, or hydrothermal activity after the peak

98 metamorphism prior to the deposition of the Athabasca Basin (Annesley and Millar 2011; Card

99 2012; Card 2013). Chemical weathering of the basement is recorded as a paleo-weathering

100 profile along the unconformity (Macdonald 1985; Adlakha et al. 2013).

101   The eastern Athabasca Basin is composed of ~500 m of fluvial quartz dominated (~99%)

102 conglomeratic sandstones, consisting of four major sequences: the lower Read formation, and the

103 Manitou Falls formations B, C and D (Fig. 1b). The sandstones contain minor hematite, dickite-

104 kaolinite, illite and Sr-Ca-SO_4^{2-}-rich aluminum phosphate sulfate (APS) minerals (e.g., Kotzer

105 and Kyser 1995; Gaboreau 2007). The regional diagenetic minerals (primarily dickite with

106 hematite) are overprinted by illite, chlorite, magnesio-foitite (alkali-deficient Mg-rich

107 tourmaline), and LREE-P rich APS minerals near the vicinity of uranium deposits and basement

108 structures (Kotzer and Kyser 1995; Gaboreau et al. 2007; Jefferson et al. 2007).

5

Local Geology

The P2 fault is a 13 km long reverse structure (~050, 45-60 SE) along graphitic metapelite of the Wollaston supergroup, which originated as a ductile structure during the Trans-Hudson Orogen. The fault underwent brittle reactivations during and after deposition of the unconformably overlying sandstones of the Athabasca Basin (e.g., McGill 1993; Hajnal et al. 2010). Vertical movement along the P2 fault is responsible for displacement of the unconformity by up to 80 m and the fault extends into the lower sandstones as splays and fractures (McGill 1993).

Extensive alteration occurs along the P2 fault zone in the basement, including the areas of mineralization and barren of mineralization (e.g., McGill 1993; Adlakha and Hattori 2015, 2016). The least altered rocks found far outside the fault zone and below the paleo-regolith consist mainly of biotite ± garnet and sillimanite gneisses and coarse-grained to pegmatitic granite lenses consisting of predominately quartz, plagioclase and K-feldspar ± mica. The earliest alteration of the basement fault is expressed as veins of oxy-dravite, graphite, pyrite, and quartz, which postdates the peak metamorphism and predates the deposition of the Athabasca Basin (Adlakha and Hattori 2016, Adlakha et al. 2017). The prevalent alteration along the fault is associated with uranium mineralization of the McArthur River deposit and comprises illite, sudoite (Al-Mg chlorite), magnesio-foitite and LREE-P rich APS minerals (Kotzer and Kyser 1995; Gaboreau et al. 2007; Alexandre et al. 2009; Ng et al. 2013; Adlakha and Hattori 2015, 2016). The assemblage also forms a halo around the ore bodies of the McArthur River deposit.

The McArthur River deposit comprises nine mineralized zones and three showings, which are structurally controlled by the P2 fault and unconformity (Fig. 1c; Bray et al. 2018). All

6

131   ore bodies are hosted within the lowermost sandstone unit of the Athabasca Basin, with the

132   exception of Zone 2 that is almost completely hosted within the basement rocks. The Zone 2 ore

133   body is additionally bound by the Vertical Quartzite (VQ) fault that runs along the contact

134   between basement quartzite and graphitic metapelite (Adlakha and Hattori 2015). The McArthur

135   River deposit is the largest high-grade uranium deposit yet discovered in the world, with an

136   average grade of ~7.14 % U_3O_8 in proven reserves (Bray et al. 2018). Low grade or sub-

137   economic mineralization, including the P2 Main deposit, is found sporadically along the fault

138   outside of the main deposit area (Fig, 1c).

Sampling and Analytical Methods

140   Eighteen samples were selected for this study, primarily based on the abundance of Ti-

141   oxide minerals observed during petrographic work and to ensure representation of all areas of the

142   P2 fault relative to the McArthur River deposit (e.g., mineralized, low-grade, apparently barren;

143   Table 1, Fig. 1c). Sixteen samples are of the basement rocks along the fault and two are of basal

144   conglomeratic sandstone of Read formation immediately above the unconformity (Table 1; Fig.

145   2).

146   Mineral identification, textural analysis and imaging were carried out using a

147   petrographic microscope in both transmitted and reflected light on polished thick (~100 μm)

148   sections, followed by a TESCAN MIRA 3 LMU Variable Pressure Schottky Field Emission

149   SEM at Saint Mary's University, Halifax, Nova Scotia, using a working distance of 17 mm and

150   accelerating voltage of 20 kV.

151   Polymorphs of Ti-oxide were distinguished using a Jobin-Yvon Horiba LabRam HR

152   confocal laser Raman microspectrometer at Saint Mary's University, Halifax, Nova Scotia.

153 Phase identification used Raman shifts at 242, 449 and 614 cm^{-1} for rutile, and 199, 400, 517

154 and 642 cm^{-1} for anatase. Analyses were performed using a 532 nm (green) Nd-YAG laser (105

155 mW laser power at objective) focused through a 100x objective lens. Spectra were collected

156 using a 600 grooves/mm grating, 50 μm confocal hole size, and Synapse 1024 x 256 pixel CCD

157 detector. Spectra collection was performed using an acquisition duration of 10s with 3

158 accumulations. Frequency calibration was performed using a pure silicon wafer.

159 The chemical composition of Ti-oxide minerals was determined by wavelength

160 dispersive X-ray spectrometry using a JEOL 8230 SuperProbe at the University of Ottawa,

161 Ottawa, Ontario. The working conditions were set to an accelerating voltage of 20 kV with a 40

162 nA beam current focussed to a 5 μm spot size. Data collection time was 40 s with 20 s

163 background time for all elements. Analytical standards include spinel [$(Cr,Mg,Al,Fe)_3O_4$ for

164 AlKα, CrKα, and MgKα], Mn columbite (NbLα), ThO_2 (ThMα), zircon (ZrLα), $NiTa_2O_6$

165 (TaMα), rutile (TiKα), cassiterite (SnLα), $CoWO_4$ (WMα), UO_2 (UMα), powellite (MoLα),

166 vanadinite (VKα), hematite (FeKα), tephroite (MnKα), and diopside (SiKα). Data reduction used

167 the ZAF program. Data for FeO were recalculated as Fe_2O_3, considering Fe in rutile is usually

168 Fe^{3+} in most environments, even in reducing conditions (e.g., Vlassopoulos et al. 1993).

169 Detection limits are listed in Appendix Tables 1 and 2. Due to the irregular shape and small size

170 of anatase crystals, Si and Al values were monitored for contamination by surrounding silicate

171 minerals.

172 Trace element abundances were determined using a Resonetics S-155-LR 193nm

173 Excimer laser ablation system coupled to an Agilent 7700x quadrupole ICP-MS at the University

174 of New Brunswick, Fredericton, New Brunswick. Detailed running conditions of the LA-ICP-

8

175   MS are listed in Appendix Table 3. All grains were examined for inclusions before analysis, and

176   time-sequence intensity graphs of the data were inspected for possible inclusions. The data were

177   imported into IGOR Pro (Version 6.3.7, Wavemetrics Inc.) and reduction was carried out using

178   the add-on Iolite (Version 2.5). The calibration standard NIST610 (National Institute of

179   Standards and Technology, synthetic glass) and ratio of each isotope to counts of ^{49}Ti (using

180   average EPMA data for Ti in Ti-oxides from each sample) were used to quantify trace element

181   abundances. Analysis of BCR-2G (Columbia River Basalt, USGS) indicates accuracy within

182   10% and precision within 5% for the trace elements. Data of the same grains using LA-ICP-MS

183   and EPMA yielded similar results for elements Nb, W, and Cr (Appendix Fig. 1). Data of V

184   produced by LA-ICP-MS yields higher values (systematically by ~1000 ppm) than EPMA.

185   **Results**

186   **Ti-oxide Polymorph Occurrences and Petrography**

187   Examination of representative grains of Ti-oxide in samples using Raman spectroscopy

188   identified two Ti-oxide polymorphs: rutile and anatase (Figs. 3a, b; Table 1). Brookite was not

189   detected in any samples. The host rocks, mineral assemblages, and paragenesis of the Ti-oxide

190   polymorphs are described below and illustrated in Figure 4.

191   Rutile occurs as a minor but common mineral in hydrothermally altered metapelite and

192   quartzite (Table 1; Fig. 5). No rutile was observed in sandstone samples. In thin section, rutile is

193   dark reddish-brown to opaque under transmitted light (Figs. 5a, b), and weakly-moderately

194   reflective light grey with a faint bluish tint in reflected light. Three types of rutile are identified

195   based on texture (Table 2). The most abundant type of rutile (Type 1) occurs as disseminated,

196   euhedral-subhedral grains ranging from 20 to 500 μm in diameter with corroded rims and

9

197   fractures (Fig. 5a). The host rocks for Type 1 rutile are mainly foliated and altered graphitic

198   metapelite with or without cm-scale leucosomes (e.g., Fig. 2a), but it also occurs in the quartzite

199   sample (MAC79). Type 1 rutile is distributed along all studied areas of the P2 fault, including the

200   areas near mineralization, such as Zones 1 (samples MAC201, 203), 2 (MAC70, 79, 84, 86, 152,

201   441, 444), 4 (MAC420), and the low-grade P2 Main deposit (MAC98, 99), as well as

202   unmineralized areas (MAC127, 426, 436) (Fig. 1c; Tables 1 and 2). Some metapelites show

203   varying degrees of early silicification (e.g., Figs. 2c, d,) where large (> 1cm) patches of anhedral

204   quartz replace metapelite. Late-stage brecciation with desilicification and alteration by light blue

205   magnesio-foitite is common in samples from both mineralized (e.g, MAC99; Fig. 2d) and

206   unmineralized areas (e.g. MAC436, Fig. 2e). Some metapelite samples are in contact with

207   anatexite (> 10 cm wide) (e.g., MAC420; Fig. 2f); although the granitic lenses do not contain Ti-

208   oxide minerals. Notably, Type 1 rutile is absent in mineralized sample MAC423 of the Zone 2

209   ore body, which contains a cm-wide vein of primary uraninite bordered by red hematite (Fig.

210   2g). Type 1 rutile does occur in sample MAC98 below the P2 Main deposit, which contains

211   veinlets of a U-oxide phase containing high Si and Ca. This phase is similar in composition to U-

212   Ca hydroxide reported by Fayek and Kyser (1997), which is considered to be a remobilization

213   product of primary uraninite.

214   Type 1 rutile is early in all samples and commonly occurs with an assemblage of oxy-

215   dravite, quartz, graphite, zircon, pyrite, and micas (biotite and/or muscovite; Figs. 4, 5a-c; Table

216   2). This assemblage occurs in veins or bands parallel with fabric of graphitic metapelite samples

217   from all areas of the fault (apparently barren and mineralized; Fig. 1c; e.g, samples MAC84, 99,

218   127, 201, 420 and 436). In these samples, disseminated rutile and graphite laths occur with, and

219   sometimes as inclusions in, sub-euhedral oxy-dravite and quartz (Figs. 5a-c). Zircon and quartz

10

220   are also found as inclusions in rutile and oxy-dravite (Fig. 5a). The micas are commonly altered

221   by chlorite. Sample MAC127 is unusual as it contains a low abundance of oxy-dravite, in

222   addition to a Mg-mineral (possibly cordierite) that is pseudomorphed by sudoite (Fig. 5b). This

223   Mg-mineral is likely an earlier metamorphic mineral as it occurs as inclusions in oxy-dravite and

224   is embayed by graphite. In other metapelite samples (e.g., MAC70, 86, 98, 127, 152, 203, 441,

225   444), the minerals that formed together with rutile are largely replaced by later clay-sized

226   minerals, except for quartz, pyrite, zircon, and graphite in some samples (MAC70, 86, 441, 444).

227   Therefore, it is difficult to determine the exact minerals that formed together with rutile in these

228   samples. In samples MAC98, 152, and 203, the only mineral preserved with rutile is quartz (Fig.

229   5d). In unbrecciated samples MAC152 and 203, feldspar grains are evident but pseudomorphed

230   by fine-grained illite, whereas feldspar grains are not recognized in brecciated and intensely

231   altered sample MAC98. In the quartzite sample (MAC79), Type 1 rutile forms subhedral to

232   anhedral intergrowths with quartz that contains acicular sillimanite crystals (Fig. 5e). Rutile and

233   quartz occur with muscovite that is coated by Fe-oxide (Fig. 5e). In this sample, euhedral zircon

234   occurs as inclusions in rutile, quartz, and muscovite.

235   The second type (Type 2) of rutile is fine-grained and blocky. It only occurs in sample

236   MAC98 from below the P2 Main deposit (Fig. 5f). This rutile occurs as inclusions with rounded

237   anatase within an altered coarse-grained mineral. The mineral is pseudomorphically replaced by

238   sudoite and dendritic to patchy anatase. The third type (Type 3) occurs as fine-grained, elongate

239   grains along cleavage planes of chloritized (Fe-Mg chlorite) muscovite and biotite in samples

240   MAC70, 84, 86, 127, 423, 441, and 444, which represent all areas of the fault (Figs. 1c, 5c).

11

241   Late clay-sized minerals are common in the studied samples and predominately consist of

242   sudoite, illite, and magnesio-foitite with or without LREE-P rich APS minerals or anatase. These

243   minerals surround and infill fractures of rutile, oxy-dravite and graphite. Magnesio-foitite forms

244   overgrowths on intergrown oxy-dravite and rutile (Figs. 5a,c,d,f). Notably, rutile in mineralized

245   sample MAC98 is fractured and coated by late secondary U-oxide (Fig. 5d).

246   Anatase is observed in samples of both sandstone and the basement (Table 2). It is opaque

247   to translucent and brown-blue in thin section under transmitted light (Fig. 6a). Anatase is

248   moderately reflective and grey in reflected light (Fig. 6b). It is distinguished from rutile in thin

249   sections by texture because anatase is usually anhedral and fine-grained with irregular grain

250   boundaries. Additionally, anatase is darker in BSE images than rutile (Fig. 5f).

251   Anatase occurs in sandstone samples of the basal Read formation in unmineralized

252   (MAC430) and low grade (MAC406) areas of the P2 fault (Fig. 1c). Both sandstone samples

253   consist of banded, fine to coarse-grained, detrital quartz with red to buff coloured interstitial clay

254   (kaolinite-group minerals and illite), due to varying amounts of fine-grained hematite (Fig. 2h).

255   Note that kaolinite-group minerals will be referred to simply as kaolin because polymorphs (i.e.

256   kaolinite vs. dickite) were not in identified this study. Titanium oxides were not observed in

257   samples of the upper sandstone units in this study (n = 5), such as those in the Manitou Falls

258   formation.

259   In both sandstone samples, anatase is concentrated in the silty layers comprising detrital

260   quartz and zircon, and authigenic minerals such as kaolin, illite, APS minerals and fine-grained

261   red hematite (Figs. 6a,b; Table 2). Anatase grains in sandstones are typically anhedral and

262   patchy, occurring in clusters and sometimes containing inclusions of Fe-oxide (Figs. 6b,c). The

12

263   anatase grains overprint diagenetic kaolin and crosscut overgrowths of detrital quartz grains,

264   which contain Sr and SO_4^{2-}-rich APS minerals (Fig. 6c). Anatase is in textural equilibrium with

265   coarse-grained (~20 μm) illite, which alters earlier kaolin (Fig. 6b).

266   The mode of occurrence for anatase varies in basement samples (e.g., MAC98, MAC423,

267   MAC426, MAC436) and is summarized in Table 2. In sample MAC98, anatase forms both

268   rounded grains (< 15 μm) and dendritic to patchy growths in the altered coarse-grained mineral

269   described above, as well as fine-grained disseminations (Fig. 5f). Based on compositional

270   similarities, both the rounded and patchy anatase are of similar origin, likely replacements of the

271   unidentified altered mineral (see next section on anatase composition). The disseminated anatase

272   occurs with stringers of hematite in the matrix of sudoite and magnesio-foitite, which are

273   overprinted by late secondary U-hydroxide. In mineralized sample MAC423, anatase occurs as

274   irregular anhedral to lath-like disseminations in clay-sized minerals near the margin of the

275   uraninite vein and is coated by secondary U-hydroxide (Fig. 6d). In sample MAC426, anatase

276   forms euhedral to anhedral coarse grains (up to 100 μm). This anatase occurs as inclusions in

277   dolomite, which is intergrown with coarse-grained and lath-like black hematite (Fig. 6a). In

278   back-scattered electron images, some anatase grains in MAC426 contain euhedral bright cores

279   reflecting high W and Fe content (Fig. 6a). In sample MAC436, anatase forms clusters of small

280   (< 15 μm), and rarely coarse, anhedral grains disseminated in fine-grained magnesio-foitite with

281   LREE-P rich APS minerals around large euhedral rutile with corroded rims (Figs. 5b, 6e,f). Both

282   latter samples are from unmineralized portions of the P2 fault.

Major and Minor Element Composition

283

284   The composition of rutile is determined using 290 EPMA measurements from 15 samples

285 (see Table 3 for the average values, and Appendix Table 1 for the entire dataset). All data are of

286 Type 1 disseminated rutile, except for 5 measurements of Type 2 rutile inclusions in the altered

287 coarse-grained mineral. Type 3 rutile is too fine-grained for accurate analysis. Type 1 rutile

288 contains variably high Nb (up to 2.70 wt.%), Fe (up to 0.78 wt.%), V (up to 1.44 wt.%) and W

289 (up to 0.51 wt.%) (Table 3). In individual samples, rutile grains are similar in composition (Table

290 3). The composition of Type 1 and 2 rutile in sample MAC98 are similar and contain

291 exceptionally high Nb (average 3.29 wt.%; Table 3). Contents of Al, Th, Sn, U, Mo, Mn and Mg

292 are close to, or lower than the detection limits of the instrument.

293   Forty-seven EPMA measurements of anatase from five samples (MAC98, 406, 426, 430,

294 436) indicate variably high Fe content (up to 0.99 wt.%; Table 4; Appendix Table 2 for the full

295 dataset). These data do not include fine-grained skeletal anatase in MAC98 or lathlike anatase in

296 MAC423 as it is commonly coated by U-oxide. Except for sample MAC426, anatase contains

297 mostly low concentrations of impure elements compared to rutile: up to 0.55 wt.% Nb, 0.06

298 wt.% Cr, 0.05 wt.% W, 0.31 wt.% V, 0.10 wt.% Al, and 0.07 wt.% Si (Table 4). Most anatase

299 grains contain low Zr (<0.13 wt.%). Contents of Mg, Mn, Mo, Sn, Ta, Th and U are below the

300 detection limits of the EPMA. Two types of anatase were analyzed in MAC98, the early rounded

301 inclusions and patchy replacements. The early anatase inclusions have high Fe (0.24 wt.%) and

302 essentially no V, whereas the patchy replacement anatase is either compositionally similar or

303 contains relatively low Fe (~0.08 wt.%) and high V (up to 0.31 wt.%). Anatase in sample

14

304   MAC426 is compositionally distinct and contains variably high Fe (up to 0.99 wt.%), W (up to

305   2.01 wt.%), Cr (up to 0.15 wt.%) and Zr (up to 0.36 wt.%).

306   **Trace Element Abundances**

307   One hundred and twenty-six measurements of rutile (Type 1) from thirteen samples and

308   fifteen measurement of anatase from five samples using LA-ICP-MS are reported. Small number

309   of anatase measurement is due to its small grain size. Average trace element concentrations of

310   rutile and anatase are listed in Tables 3 and 4, respectively (see Appendix Tables 5 and 6,

311   respectively, for full data sets).

312   Trace element data show that rutile contains variable Ca (up to 120 ppm), Sc (5.8 to 1050

313   ppm), Co (up to 102 ppm), Se (up to 170 ppm) Sn (up to 440 ppm), Hf (up to 178 ppm), Th (up

314   to 44 ppm), and U (up to 126 ppm). Rutile contains low Mo (<33 ppm), Y (<21 ppm) and Pb

315   (<7.4 ppm).

316   Anatase contains variable concentrations of Ca (up to 9760 ppm), Sn (up to 130 ppm), Hf

317   (up to 160 ppm), Ta (up to 190 ppm), Th (up to 68.7 ppm), Pb (up to 32 ppm) and U (up to 180

318   ppm). Anatase contains low concentrations of Ga (<2.59 ppm), Y (<9.5 ppm), and Mo (<8.8

319   ppm).

320   **Discussion**

321   **Crystal Chemistry of Ti-Oxide Minerals**

322   Rutile consists of chains of TiO_6^{8-} octahedra that share two edges and extend parallel to

323   the c-axis (Klein and Dutrow 2007). Adjacent octahedral chains are linked through sharing of a

324   single O, with each O in triangular coordination with Ti. Rutile in this study shows extensive

15

325 substitution of Ti with Fe, V, and Nb (Table 3). While tetravalent cations can undergo simple

326 substitution with Ti ($M^{4+} \leftrightarrow Ti^{4+}$), non-tetravalent cations in rutile are commonly accommodated

327 by coupled substitutions: $M^{2+} + M^{6+} \leftrightarrow 2Ti^{4+}$, $M^{3+} + M^{5+} \leftrightarrow 2Ti^{4+}$, $M^{2+} + 2M^{5+} \leftrightarrow 3Ti^{4+}$, and

328 $2M^{3+} + 2M^{6+} \leftrightarrow 3Ti^{4+}$ (e.g., Urban et al. 1992; Scott and Radford 2007).

329   Previous studies indicate Fe^{2+}, Fe^{3+}, V^{3+}, and V^{4+} are compatible with rutile (e.g. Urban et

330 al. 1992). The oxidation state of Fe and V in rutile of this study and their substitution

331 mechanisms are evaluated using biplots (Fig. 7). The slope of Ti and V range from -1 to -½,

332 reflecting V^{4+} substituting for Ti^{4+} in some rutile (Fig. 7a; e.g., MAC70, 84, 86, 127) and V^{3+} in

333 others (e.g., MAC79, 98, 99, 201, 203, 420). The V and Nb contents of rutile containing V^{3+}

334 exhibit a slope of 1 (Fig. 7b), suggesting V^{3+} is accommodated by coupled substitution with Nb^{5+}

335 ($V^{3+} + Nb^{5+} \leftrightarrow 2Ti^{4+}$). Iron in rutile is generally considered to be Fe^{3+} (Vlassopoulos et al. 1993

336 and references therein). Iron and Nb in some rutile show a slope between 1 and ½, suggesting

337 variable valence of Fe (Fig. 7c). Many rutile grains contain high Nb relative to Fe, as the data

338 trends plot below the ½ sloped line without intersecting 0 (Fig. 7c). This is explained by coupled

339 substitution of Nb with minor amounts of other trivalent elements, such as V^{3+}, Cr^{3+}, and Al^{3+}

340 (Fig. 7d)

341   The V^{4+}-bearing rutile grains have relatively high V content, compared to V^{3+}-bearing

342 rutile. This likely reflects the compatibility of V^{4+} over V^{3+} in rutile, considering V^{4+} has the

343 same charge and is similar in size in 6-fold coordination (0.78 Å for V^{3+} vs. 0.72 for V^{4+}) to Ti^{4+}

344 (0.745 Å). Except for rutile from MAC98, V^{3+}-bearing rutile contains relatively lower V and

345 higher Fe and Nb (Fig. 7d). The compositional difference between these two rutile types may be

16

346   attributed to varying fO$_2$, where V^{4+} is preferentially incorporated into rutile over Fe and Nb

347   under oxidizing conditions.

348   Anatase, like rutile, consists of Ti in octahedral coordination with O, and O in triangular

349   coordination with Ti. In anatase, the Ti octahedra share edges with four adjacent octahedral

350   (Klein and Dutrow 2007). Anatase contains variably high Fe, with lesser V, Nb and W (Table 4).

351   Vanadium and Ti in V-rich anatase of MAC98 show a correlation with a slope of -1 suggesting

352   the occurrence of V as V^{4+} (Fig. 8a). Iron and Nb show a large scatter (Fig. 8b) Notably, anatase

353   of MAC426 shows a broad correlation between W and Fe with a slope of 2 (Fig. 8c), suggesting

354   Fe^{3+} and W^{6+} (2Fe^{3+} + W$^{6+} \leftrightarrow$ 3Ti^{4+}). The oxidized state of Fe in anatase is also supported by

355   abundant hematite in the samples (Figs. 4, 5f, 6a).

356   The majority of Fe in anatase is not charge balanced by other cations, such as Nb (Fig.

357   8b) and W (Fig. 8c). High Fe^{3+} may be attributed to microinclusions of hematite, which were

358   observed in sandstone-hosted anatase. Inverse correlations between Ti and Fe with a slope of 1

359   for both sandstone and basement hosted anatase can be explained by contamination of the EPMA

360   data with hematite (Fig. 8d); however, hematite inclusions were not observed in the basement

361   anatase. It is possible these anatase contain nano-inclusions that were obvious using SEM.

362   Alternatively, a substantial amount of OH$^-$ may occur in the O^{2-} site of Ti-oxides to compensate

363   the substitution of trivalent cations (M^{3+} + OH$^- \leftrightarrow$ Ti^{4+} + O^{2-}; e.g., Soffer 1961, Vlassopoulos et

364   al. 1993, Tompsett et al. 1995, Swope et al. 1995, Smyth 2006). Therefore, it is possible that OH$^-$

365   may charge balance Fe^{3+}. Unfortunately, the presence of OH- is not confirmed as it is not

366   detectable by the methods used in this study. The mechanism for high Fe^{3+} in anatase remains

367 unresolved, but hematite microinclusions, and possibly nanoinclusions, are the most likely

368 explanation at this point.

The Origin of Ti-oxide Minerals Along the P2 Fault

370 The origin of Ti-oxide phases along the P2 fault is evaluated using mineral textures,

371 assemblages, and mineral composition.

372 **Rutile.** Three texturally distinct types of rutile occur in basement samples (Table 2; Fig. 4).

373 Type 1 rutile in graphitic metapelite and quartzite occurs with different mineral associations,

374 suggesting its crystallization during multiple events. Type 2 rutile is rare, occurring only in

375 sample MAC98. Considering it is essentially identical in composition with Type 1 rutile (Table

376 3), the two types of rutile in this sample are considered to be of similar origin. Type 3 rutile is

377 similar in texture to needle-like rutile in chloritized biotite laths observed in the basement rocks

378 outside the P2 fault (Adlakha et al. 2013). The Type 3 rutile likely shares a similar origin, which

379 is interpreted to be an alteration product of mica during retrograde metamorphism (Adlakha et al.

380 2013).

381 Textural evidence indicates that Type 1 rutile pre-dates the low temperature basinal

382 hydrothermal activity that formed magnesio-foitite, sudoite, and illite ± uraninite (Figs. 4, 5).

383 This is evident from the textural equilibrium between rutile and oxy-dravite, which are both

384 surrounded by magnesio-foitite (Fig. 5a; Adlakha and Hattori 2016). In samples without oxy-

385 dravite, fractures of rutile are filled with the late alteration minerals listed above. Both rutile and

386 oxy-dravite must have rystallized before deposition of the Athabasca Basin considering oxy-

387 dravite occurs as a detrital mineral in the Athabasca sandstones (Mercadier et al. 2012, Adlakha

388 and Hattori 2016). Therefore, the possible origins of this Type 1 rutile include: i) detrital origin

18

389   (pre-metamorphism of the basement), ii) crystallization during metamorphism of the basement,

390   or iii) post-peak metamorphic hydrothermal crystallization.

391   A detrital origin is consistent with the rounded shape of some Type 1 rutile grains, such

392   as those abundant in sample MAC436 (Fig. 5e). The common association of rutile in this study

393   with other "heavy minerals" such as tourmaline and zircon (e.g., MAC99, MAC436; Figs. 5a,6e)

394   also supports the detrital origin. If they are indeed detrital, they must have recrystallized and/or

395   underwent Ostwalt ripening in order to achieve such large grain sizes during later metamorphism

396   and hydrothermal activity. Their composition would have likely been modified during these later

397   processes.

398   During metamorphism and hydrothermal activity, Ti is generally immobile (Ayers and

399   Watson 1993). Therefore, both metamorphic and hydrothermal rutile forms through the

400   breakdown or alteration of precursor Ti-bearing minerals, such as biotite, rutile, ilmenite, titanite,

401   titaniferous magnetite, and Ti-rich amphibole (e.g., Schwartz 1958; Luvizotto and Zack 2009;

402   Meinhold et al. 2010). Type 1 rutile of this study exhibit euhedral to ovoid disseminated grains,

403   similar to those reported in other high-grade metamorphic rocks (e.g. Meinhold et al. 2010).

404   However, we suggest its formation during multiple events based on its mineral association.

405   Rutile incorporates high-field strength elements (HFSE; Nb, Ta, Zr, Hf, U and Th), and

406   their ratios may help constrain its origin (Bau 1996; Luvizotto and Zack 2009; Carocci et al.

407   2019; Pereira et al. 2019; Zeh et al. 2018; Plasva et al. 2018). For example, rutile formed from

408   the breakdown of Ti-bearing minerals, such as biotite and ilmenite, during high grade

409   metamorphism inherits variably high Nb/Ta ratios (Figs. 9a, b; Luvizotto and Zack 2009; Meyer

410   et al. 2011; Stepanov and Hermann 2013). On the other hand, rutile formed from hydrothermal

19

411   fluids show characteristically low Nb/Ta ratios and high Ta (Carruzzo et al. 2006; Dostal et al.

412   2009). The fractionation of Ta from Nb in aqueous fluids is attributed to a variety of reasons,

413   including the availability of ligands forming soluble complexes (e.g., Bau et al. 1996), and the

414   preferential incorporation of one element into other minerals (e.g., Dostal et al. 2000).

415   The Nb/Ta ratios of Type 1 rutile in this study are between 5 to 24 (average 13 ± 6, 1σ;

416   Fig. 9a), which bracket the value for average continental crust (12.4; Fig 9b; Rudnick and Gao,

417   2003). The majority of samples show an inverse relationship between Nb/Ta and Ta, which is

418   consistent with rutile in pelitic rocks that formed during high grade metamorphism (Luvizotto

419   and Zack 2009; Meyer et al. 2011; Figs. 9a,b). Therefore, high Nb/Ta ratios of the majority of

420   rutile grains suggest a metamorphic origin. However, some low values correspond with high Ta

421   and do not follow the trend, suggesting a different origin. As previously mentioned, rutile with

422   low Nb/Ta ratios and high Ta characterizes hydrothermal rutile. In addition, the low Nb/Ta rutile

423   grains are from samples containing different mineral assemblages, including MAC99 with oxy-

424   dravite, quartzite of MAC79, and highly altered samples MAC98, 203, and 441 (Table 2). The

425   different mineralogy of these samples suggest that they were not formed during a single

426   hydrothermal event. Notably, recent studies propose that the quartz-rich and tourmaline-graphite-

427   pyrite rich rocks, similar to those that contain this rutile, are products of pre-Athabasca

428   hydrothermal activity after the peak metamorphism of the basement (Annesley and Millar 2011;

429   Card 2012; Adlakha and Hattori 2016).

430   The Zr/Hf ratios of rutile of metamorphic and hydrothermal origine may be distinct,

431   where the former exhibits higher ratios than the latter (Fig. 9b; Luvizotto and Zack 2009; Meyer

432   et al. 2011; Pereira et al. 2019). The Zr/Hf ratios of rutile in this study show low variability

20

433 (average 18 ± 2, 1σ) and overlap with both metamorphic and hydrothermal rutile elsewhere (Fig.

434 9b). Considering the common occurrence of zircon in our samples, the Zr/Hf ratios of rutile in

435 our samples are likely controlled by zircon (Figs. 5c,e).

436 Type 1 rutile is characterized by low Th (commonly less than the detection limit of the

437 ICP-MS) and variably high U (9.06 to 126 ppm; Fig. 9c). This is consistant with the

438 incompatibility of Th rutile (usually <0.5 ppm) due to its large ionic radius (Brenan et al. 1994;

439 Klemme et al., 2005). Hexavalent U is compatible with rutile (Brenan et al. 1994) and high U is

440 common for rutile in metapelitic rocks (Zack and Kooijman 2017). Accordingly, the rutile of a

441 suspected metamorphic origin (i.e. those with high Nb/Ta ratios such as in MAC84, 86, 127, and

442 152; Fig 9a) contains relatively high U (Fig. 9c). The basement rocks below the Athabasca Basin

443 are notably rich in U (e.g., Hecht and Cuney, 2000), and interaction of fluids with such rocks

444 could also explain high U in rutile. Considering U is soluble as U^{6+} in oxidizing aqueous fluids,

445 high U in hydrothermal rutile likely indicates oxidizing conditions of the fluids, whereas low U

446 indicates reduced fluids. Interestingly, the suspected hydrothermal rutile (high Ta with low

447 Nb/Ta ratios (e.g., MAC79, 98, 99, 203, 436 and 441) contains relatively low U, which may

448 indicate their formation or recrystallization by fluids in reduced oxidation conditions. The

449 formation of these rutile under reduced conditions is supported by the occurrence of V as

450 reduced V^{3+} (e.g., MAC79, 98, 99, 203; Figs. 7a,d). Figure 9d, a biplot of the ratios of V/Nb

451 versus Fe/V, demonstrates that rutile with V^{3+} contains high Nb and Fe, whereas rutile with high

452 V^{4+} contains low Nb and Fe. The relative abundance of U, V, Nb, and Fe may be useful to

453 qualitatively indicate the oxidation conditions during the formation of different generations of

454 rutile. (Figs. 9c, d).

21

455   **Anatase.** Anatase of this study occurs in the hematitized basal sandstone and basement.

456 In the sandstone samples, anatase crosscuts the early diagenetic assemblage of quartz

457 overgrowths with kaolin and Sr-rich APS minerals, suggesting anatase crystallization during late

458 diagenesis or early hydrothermal activity. Since the phase transformation of rutile to anatase is

459 not thermodynamically favorable (Osborn 1953; Smith et al. 2009), we suggest that anatase

460 crystallized through dissolution of Ti-bearing detrital minerals, such as rutile, at relatively low

461 temperatures. Titanium is soluble in highly acidic fluids (e.g., Vikre and John, 2010; Pe-Piper et

462 al. 2011), which prevailed during the diagenesis and subsequent uraniferous hydrothermal

463 activity in Athabasca Basin (e.g., Kister et al. 2005). The original detrital mineralogy of the

464 sandstones is largely affected by the diagenetic-hydrothermal assemblages and even relatively

465 insoluble detrital minerals such as tourmaline, monazite and zircon show partial dissolution (e.g.,

466 Fayek and Kyser 1997; Gaboreau 2007; Adlakha and Hattori 2016).

467   Anatase in the basement occurs near uranium mineralization and in apparently barren

468 areas (Table 1; Fig. 1c). In these samples, disseminated anatase is typically fine-grained (< 15

469 μm) and associated with magnesio-foitite, sudoite, illite, and overprinted by late U-hydroxide.

470 The textural evidence suggests anatase crystallized together with magnesio-foitite, sudoite, and

471 illite. We suggest that anatase of the basement forms from the dissolution of Ti-bearing minerals

472 (e.g., rutile and mica), considering the occurrence of fine-grained anatase disseminated around

473 rutile with corroded rims (Fig. 6e). Additionally, lath-like anatase near the uranium

474 mineralization likely pseudomorph mica (Fig. 6d) and skeletal and patchy anatase overprint the

475 unknown coarse-grained mineral (Fig. 4f). In the basement, anatase also forms subhedral-

476 euhedral inclusions in late dolomite with coarse-grained hematite (Fig. 6a). This anatase is likely

477 derived from the alteration of Ti-bearing minerals of the wallrock. Although veins of dolomite

22

478 and quartz are found proximal to uranium deposits (e.g., Kotzer and Kyser 1995, Derome et al.

479 2005), this particular sample (MAC426) occurs in an apparently barren area (Fig. 1c), ~80 m

480 below the unconformity. Considering anatase i) occurs with hematite in both sandstone and

481 basement samples, ii) post-dates the diagenetic assemblage of the sandstones, and iii) is coeval

482 with magnesio-foitite, sudoite and illite in the basement, we suggest the protracted crystallization

483 of anatase in both rock types by oxidizing and acidic hydrothermal fluids from the basin shortly

484 after diagenesis and during hydrothermal activity related to uranium mineralization (Fig. 4).

485 To the best of the authors' knowledge, no study has been conducted on the partitioning of

486 elements between anatase and fluids. Based on EPMA data, anatase of this study generally

487 contains lower concentrations of impurities than rutile, except for variably high Fe in most

488 anatase and high Fe and W in anatase of MAC426 (Figs. 7, 9d). These data are consistent with

489 anatase compositions reported elsewhere (e.g. Triebold et al. 2011; Plavsa et al. 2018).

490 Considering that anatase commonly occurs with hematite (Table 1; Figs. 2g-h, 5h-i), it is

491 unsurprising that anatase contains high Fe^{3+}. The low concentrations of other elements may

492 reflect the relatively low temperature of anatase crystallization, as low temperatures deter

493 incorporation of impurities. Furthermore, adjacent Ti-O octahedra in anatase share four edges

494 compared with two in rutile (Klein and Dutrow 2007). This may restrict the substitution of large

495 and/or highly charged cations in anatase.

496 Anatase of this study shows similar Nb/Ta ratios as rutile with variable Zr/Hf ratios, and

497 contents of U and Th depend on host rock (e.g., basement vs. sandstone; Figs. 9a-c). The Nb/Ta

498 ratios are likely inherited from precursor rutile. Sandstone-hosted anatase shows variably high

499 Zr/Hf ratios (up to 39; open diamond markers in Fig. 9b). Since Zr and Hf are mostly hosted by

23

500   zircon, they are likely transferred to anatase during the partial dissolution of detrital zircon. The

501   Zr/Hf ratios of detrital zircon are estimated to average $37 \pm 10(1\sigma)$, based on whole rock data of

502   the Athabasca sandstones compiled by Wright et al. (2015) (n = 8418; data filtered for U = 0 to 3

503   ppm, Zr and Hf > 0). These whole rock ratios are similar to those of anatase in sandstones,

504   confirming our proposed interpretation. Anatase in metapelite predominately exhibits low Zr/Hf

505   ratios (≤ 23, filled diamond markers in Fig. 9b), similar to the basement-hosted rutile except for

506   one grain of anatase from MAC98 with a very high value of 61. Sandstone hosted anatase

507   contains high U (up to 181 ppm) and surprisingly very high Th contents (up to 47 ppm). High U

508   content likely reflect the presence of U^{6+} in the oxidizing basinal fluids of the Athabasca Basin.

509   High Th in anatase is confirmed to be in the crystal structure based on microtextures and LA-

510   ICP-MS spectra. While high Th content in Ti-oxide is unusual, high Th is reported for authigenic

511   rutile in sedimentary rocks elsewhere (Dunkl and von Eynatten 2009). Since sandstones

512   generally contain high Th/U compared to mudstones, high Th in anatase may reflect a

513   contribution from sandstones.

514   **Implications**

515   Titanium oxides along a major fault within and below the eastern Athabasca Basin record

516   a protracted geological history. Early rutile in graphitic metapelite and quartzite of the basement

517   formed through recrystallization of fine-grained detrital rutile during regional metamorphism and

518   hydrothermal activity prior to the deposition of the Athabasca sandstones. The relative

519   abundance of U, Fe, V, Nb and Ta of rutile discriminate rutile of different origin (e.g.

520   metamorphic vs. hydrothermal) and qualitatively indicate oxidation conditions during its

521   crystallization. After sedimentation and diagenesis of the sandstones, acidic basinal fluids

522 formed anatase in sandstones and the basement at the expense of rutile and other Ti-bearing

523 minerals. The composition of anatase in sandstone records the presence of oxidizing uraniferous

524 basinal fluids. The presence of anatase in basement rocks records the incursion of basin fluids

525 into the basement, marking the onset of hydrothermal activity related to the McArthur River

526 uranium deposit. The results of this study confirm that Ti-oxides are useful in unraveling the

527 geological history of an area that underwent prolonged hydrothermal activity.

540   **References**

541 Adlakha, E. E., Hattori, K., Zaluski, G., Kotzer, T., Potter, E. G., and File, O. (2013) Alteration

542 within the basement rocks associated with the P2 fault and the McArthur River uranium deposit,

543 Athabasca Basin. Geological Survey of Canada Open File Report, 7462, 33.

25

544   Adlakha, E. E., and Hattori, K. (2015) Compositional variation and timing of aluminum

545   phosphate-sulfate minerals in the basement rocks along the P2 fault and in association with the

546   McArthur River uranium deposit, Athabasca Basin, Saskatchewan, Canada. American

547   Mineralogist, 100, 1386-1399.

548   Adlakha, E. E., and Hattori, K. (2016) Paragenesis and composition of tourmaline types along

549   the P2 fault and McArthur River uranium deposit, Athabasca Basin, Canada. The Canadian

550   Mineralogist, 54, 661-679.

551   Adlakha, E. E., Hattori, K., Davis, W. J., and Boucher, B. (2017) Characterizing fluids

552   associated with the McArthur River U deposit, Canada, based on tourmaline trace element and

553   stable (B, H) isotope compositions. Chemical Geology, 466, 417-435.

554   Agangi, A., Reddy, S. M., Plavsa, D., Fougerouse, D., Clark, C., Roberts, M., and Johnson, T. E.

555   (2019) Antimony in rutile as a pathfinder for orogenic gold deposits. Ore Geology Reviews, 106,

556   1-11.

557   Alexandre, P., Kyser, K., Polito, P., and Thomas, D. (2005) Alteration mineralogy and stable

558   isotope geochemistry of Paleoproterozoic basement-hosted unconformity-type uranium deposits

559   in the Athabasca Basin, Canada. Economic Geology, 100, 1547-1563.

560   Alexandre, P., Kyser, K., and Jiricka, D. (2009) Critical geochemical and mineralogical factors

561   for the formation of unconformity-related uranium deposits: comparison between barren and

562   mineralized systems in the Athabasca Basin, Canada. Economic Geology, 104, 413-435.

563   Alexandre, P., Kyser, K., Jiricka, D., and Witt, G. (2012) Formation and evolution of the

564   Centennial unconformity-related uranium deposit in the south-central Athabasca Basin, Canada.

565   Economic Geology, 107, 385-400.

566   Annesley, I. R., Madore, C., and Portella, P. (2005) Geology and thermotectonic evolution of the

567   western margin of the Trans-Hudson Orogen: evidence from the eastern sub-Athabasca

568   basement, Saskatchewan. Canadian Journal of Earth Sciences, 42, 573-597.

569   Annesley, I. R., and Millar, R. (2011) Tourmaline-and sulfide-bearing graphitic pelitic gneisses

570   of the Paleoproterozoic Wollaston Group, northern Saskatchewan: new insights into

571   understanding the carbon-sulfur-boron-uranium geochemical system with implications for U/C-

572   type uranium deposits. Proceedings of the 25th International Applied Geochemistry Symposium.

573   Ayers, J. C., and Watson, E. B. (1993) Rutile solubility and mobility in supercritical aqueous

574   fluids. Contributions to Mineralogy and Petrology, 114, 321-330.

575   Bau, M. (1996) Controls on the fractionation of isovalent trace elements in magmatic and

576   aqueous systems: evidence from Y/Ho, Zr/Hf, and lanthanide tetrad effect. Contributions to

577   Mineralogy and Petrology, 123, 323-333.

578   Bray, L., Murdock, G. M., and Renaud, A. D. (2018) McArthur River Operation Northern

579   Saskatchewan, Canada. National Instrument 43-101 Technical Report, 141.

580   Brenan, J. M., Shaw, H. F., Phinney, D. L., and Ryerson, F. J. (1994) Rutile-aqueous fluid

581   partitioning of Nb, Ta, Hf, Zr, U and Th: implications for high field strength element depletions

582   in island-arc basalts. Earth and Planetary Science Letters, 128, 327-339.

583   Card, C. D. (2012) The origins of anomalously graphitic rocks and quartzite ridges in the

584   basement to the southeastern Athabasca Basin. Summary of Investigations, 2, 2012-2014.

585   Card, C. D. (2013) Altered pelitic gneisses and associated "quartzite ridges" beneath the

586   southeastern Athabasca Basin: alteration facies and their relationship to uranium deposits along

587   the Wollaston-Mudjatik transition. Summary of Investigations, 2, 2013-2014.

588   Carocci, E., Marignac, C., Cathelineau, M., Truche, L., Lecomte, A., and Pinto, F. (2019) Rutile

589   from Panasqueira (Central Portugal): An Excellent Pathfinder for Wolframite Deposition.

590   Minerals, 9, 9.

591   Carruzzo, S., Clarke, D. B., Pelrine, K. M., and MacDonald, M. A. (2006) Texture, composition,

592   and origin of rutile in the South Mountain Batholith, Nova Scotia. The Canadian Mineralogist,

593   44, 715-729.

594   Černý, P., Chapman, R., Göd, R., Niedermayr, G., and Wise, M. A. (1989) Exsolution

595   intergrowths of titanian ferrocolumbite and niobian rutile from the Weinebene spodumene

596   pegmatites, Carinthia, Austria. Mineralogy and Petrology, 40, 197-206.

597   Cloutier, J., Kyser, K., Olivo, G. R., Alexandre, P., and Halaburda, J. (2009) The Millennium

598   uranium deposit, Athabasca Basin, Saskatchewan, Canada: an atypical basement-hosted

599   unconformity-related uranium deposit. Economic Geology, 104, 815-840.

600   Cloutier, J., Kyser, K., Olivo, G. R., and Alexandre, P. (2010) Contrasting patterns of alteration

601   at the Wheeler River area, Athabasca Basin, Saskatchewan, Canada: Insights into the apparently

602   uranium-barren Zone K alteration system. Economic Geology, 105, 303-324.

603 Cloutier, J., Kyser, K., Olivo, G. R., and Brisbin, D. (2011) Geochemical, isotopic, and

604 geochronologic constraints on the formation of the Eagle Point basement-hosted uranium

605 deposit, Athabasca Basin, Saskatchewan, Canada and recent remobilization of primary uraninite

606 in secondary structures. Mineralium Deposita, 46, 35-56.

607 Corrigan, D., Pehrsson, S., Wodicka, N., and De Kemp, E. (2009) The Palaeoproterozoic Trans-

608 Hudson Orogen: a prototype of modern accretionary processes. Geological Society, London,

609 Special Publications, 327, 457-479.

610 Curnan, M. T., and Kitchin, J. R. (2015) Investigating the energetic ordering of stable and

611 metastable TiO2 polymorphs using DFT+ U and hybrid functionals. The Journal of Physical

612 Chemistry C, 119, 21060-21071.

613 Dachille, F., Simons, P. Y., and Roy, R. (1968) Pressure-temperature studies of anatase,

614 brookite, rutile and TiO2-II. American Mineralogist: Journal of Earth and Planetary Materials,

615 53, 1929-1939.

616 Dachille, F., Simons, P. Y., and Roy, R. (1969) Pressure-temperature studies of anatase,

617 brookite, rutile and TiO2 (II): A reply. American Mineralogist: Journal of Earth and Planetary

618 Materials, 54, 1481-1482.

619 Derome, D., Cathelineau, M., Cuney, M., Fabre, C., Lhomme, T., and Banks, D. A. (2005)

620 Mixing of sodic and calcic brines and uranium deposition at McArthur River, Saskatchewan,

621 Canada: a Raman and laser-induced breakdown spectroscopic study of fluid inclusions.

622 Economic Geology, 100, 1529-1545.

623 Dostal, J., and Chatterjee, A. K. (2000) Contrasting behaviour of Nb/Ta and Zr/Hf ratios in a

624 peraluminous granitic pluton (Nova Scotia, Canada). Chemical Geology, 163, 207-218.

625 Dunkl, I., and von Eynatten, H. (2009) Anchizonal-hydrothermal growth and (U-Th)/He dating

626 of rutile crystals in the sediments of Hawasina window, Oman. Geochimica et Cosmochimica

627 Acta Supplement, 73, A314.

628 Fayek, M., and Kyser, T. K. (1997) Characterization of multiple fluid-flow events and rare-earth-

629 element mobility associated with formation of unconformity-type uranium deposits in the

630 Athabasca Basin, Saskatchewan. The Canadian Mineralogist, 35, 627-658.

631 Gaboreau, S., Cuney, M., Quirt, D., Beaufort, D., Patrier, P., and Mathieu, R. (2007)

632 Significance of aluminum phosphate-sulfate minerals associated with U unconformity-type

633 deposits: The Athabasca basin, Canada. American Mineralogist, 92, 267-280.

634 Gribb, A. A., and Banfield, J. F. (1997) Particle size effects on transformation kinetics and phase

635 stability in nanocrystalline TiO2. American Mineralogist, 82, 717-728.

636 Hajnal, Z., White, D.J., Takacs, E., Gyorfi, I., Annesley, I.R., Wood, G., O'Dowd, C. and

637 Nimeck, G. (2010) Application of modern 2-D and 3-D seismic-reflection techniques for

638 uranium exploration in the Athabasca Basin. Canadian Journal of Earth Sciences, 47, 761-782.

639 Hecht, L., and Cuney, M. (2000) Hydrothermal alteration of monazite in the Precambrian

640 crystalline basement of the Athabasca Basin (Saskatchewan, Canada): implications for the

641 formation of unconformity-related uranium deposits. Mineralium Deposita, 35, 791-795.

642 Hoeve, J., and Sibbald, T. I. I. (1978) On the genesis of Rabbit Lake and other unconformity-

643 type uranium deposits in northern Saskatchewan, Canada. Economic Geology, 73, 1450-1473.

644   Jamieson, J. C., and Olinger, B. (1969) Pressure-temperature studies of anatase, brookite rutile,

645   and Ti02 (II): A discussion. American Mineralogist: Journal of Earth and Planetary Materials,

646   54, 1477-1481.

647   Jefferson, C. W., Thomas D. J., Gandhi, S. S., Ramaekers, P., Delaney, G., Brisbin, D., ... and

648   Olson, R. A. (2007) Unconformity-associated uranium deposits of the Athabasca basin,

649   Saskatchewan and Alberta; in EXTECH IV: Geology and Uranium EXploration TECHnology of

650   the Proterozoic Athabasca Basin, Saskatchewan and Alberta. Geological Survey of Canada

651   Bulletin, 588, 23-67.

652   Kister, P., Vieillard, P., Cuney, M., Quirt, D., and Laverret, E. (2005) Thermodynamic

653   constraints on the mineralogical and fluid composition evolution in a clastic sedimentary basin:

654   the Athabasca Basin (Saskatchewan, Canada). European Journal of Mineralogy, 17, 325-342.

655   Klein, C., Dutrow, B., and Dana, J. D. (2007) The 23rd edition of the manual of mineral science,

656   716 p. Wiley, New Jersey.

657   Klemme, S., Prowatke, S., Hametner, K., and Günther, D. (2005) Partitioning of trace elements

658   between rutile and silicate melts: implications for subduction zones. Geochimica et

659   Cosmochimica Acta, 69, 2361-2371.

660   Kotzer, T. G., and Kyser, T. K. (1995) Petrogenesis of the Proterozoic Athabasca Basin, northern

661   Saskatchewan, Canada, and its relation to diagenesis, hydrothermal uranium mineralization and

662   paleohydrogeology. Chemical Geology, 120, 45-89.

663   Levchenko, A. A., Li, G., Boerio-Goates, J., Woodfield, B. F., and Navrotsky, A. (2006) TiO2

664   stability landscape: Polymorphism, surface energy, and bound water energetics. Chemistry of

665   Materials, 18, 6324-6332.

666   Luvizotto, G. L., and Zack, T. (2009) Nb and Zr behavior in rutile during high-grade

667   metamorphism and retrogression: an example from the Ivrea–Verbano Zone. Chemical Geology,

668   261, 303-317.

669   Macdonald, C., Sibbald, T. I. I., and Petruk, W. (1985) Mineralogy and geochemistry of the sub-

670   Athabasca regolith near Wollaston Lake. Geology of Uranium Deposits: Canadian Institute of

671   Mining and Metallurgy Special, 32, 155-158.

672   McGill, B. (1993) The P2 north uranium deposit Saskatchewan, Canada. Explo. Mining Geol., 2,

673   321-331.

674   Mei, A., Li, X., Liu, L., Ku, Z., Liu, T., Rong, Y., Xu, M., Hu, M., Chen, J., Yang, Y. and

675   Grätzel, M. (2014) A hole-conductor–free, fully printable mesoscopic perovskite solar cell with

676   high stability. Science, 345, 295-298.

677   Meinhold, G. (2010) Rutile and its applications in earth sciences. Earth-Science Reviews, 102, 1-

678   28.

679   Mercadier, J., Richard, A., & Cathelineau, M. (2012). Boron-and magnesium-rich marine brines

680   at the origin of giant unconformity-related uranium deposits: $\delta11B$ evidence from Mg-

681   tourmalines. Geology, 40(3), 231-234.

682   Meyer, M., John, T., Brandt, S., and Klemd, R. (2011) Trace element composition of rutile and

683   the application of Zr-in-rutile thermometry to UHT metamorphism (Epupa Complex, NW

684   Namibia). Lithos, 126, 388-401.

685   Morad, S. (1986) SEM study of authigenic rutile, anatase and brookite in Proterozoic sandstones

686   from Sweden. Sedimentary Geology, 46, 77-89.

687   Morad, S., and Aldahan, A. L. A. (1986) Alteration of detrital Fe-Ti oxides in sedimentary rocks.

688   Geological Society of America Bulletin, 97, 567-578.

689   Navrotsky, A. (2003) Energetics of nanoparticle oxides: interplay between surface energy and

690   polymorphism. Geochemical Transactions, 4, 34.

691   Ng, R., Alexandre, P., and Kyser, K. (2013) Mineralogical and geochemical evolution of the

692   unconformity-related McArthur River Zone 4 orebody in the Athabasca Basin, Canada:

693   implications of a silicified zone. Economic Geology, 108, 1657-1689.

694   Osborn, E. F. (1953) Subsolidus reactions in oxide systems in the presence of water at high

695   pressures. Journal of the American Ceramic Society, 36, 147-151.

696   Pe-Piper, G., Karim, A., and Piper, D. J. (2011) Authigenesis of titania minerals and the mobility

697   of Ti: new evidence from pro-deltaic sandstones, Cretaceous Scotian Basin, Canada. Journal of

698   Sedimentary Research, 81, 762-773.

699   Pereira, I., Storey, C., Darling, J., Lana, C., and Alkmim, A. R. (2019) Two billion years of

700   evolution enclosed in hydrothermal rutile: Recycling of the São Francisco Craton Crust and

701   constraints on gold remobilisation processes. Gondwana Research, 68, 69-92.

702   Plavsa, D., Reddy, S. M., Agangi, A., Clark, C., Kylander-Clark, A., and Tiddy, C. J. (2018)

703   Microstructural, trace element and geochronological characterization of TiO2 polymorphs and

704   implications for mineral exploration. Chemical Geology, 476, 130-149.

705   Rabbia, O. M., Hernández, L. B., French, D. H., King, R. W., and Ayers, J. C. (2009) The El

706   Teniente porphyry Cu–Mo deposit from a hydrothermal rutile perspective. Mineralium Deposita,

707   44, 849.

708   Ranade, M. R., Navrotsky, A., Zhang, H. Z., Banfield, J. F., Elder, S. H., Zaban, A., ... and

709   Whitfield, H. J. (2002) Energetics of nanocrystalline TiO2. Proceedings of the National

710   Academy of Sciences, 99, 6476-6481.

711   Reid, K. D., Ansdell, K., Jiricka, D., Witt, G., and Card, C. (2014) Regional setting, geology, and

712   paragenesis of the Centennial unconformity-related uranium deposit, Athabasca Basin,

713   Saskatchewan, Canada. Economic Geology, 109, 539-566.

714   Rudnick, R. L., and Gao, S. (2003) Composition of the continental crust. Treatise on

715   geochemistry, 3, 659.

716   Schandl, E. S., Davis, D. W., and Krogh, T. E. (1990) Are the alteration halos of massive sulfide

717   deposits syngenetic? Evidence from U-Pb dating of hydrothermal rutile at the Kidd volcanic

718   center, Abitibi subprovince, Canada. Geology, 18, 505-508.

719   Schwartz, G. M. (1958) Alteration of biotite under mesothermal conditions. Economic Geology,

720   53, 164-177.

721   Scott, K. M. (2005) Rutile geochemistry as a guide to porphyry Cu–Au mineralization,

722   Northparkes, new South Wales, Australia. Geochemistry: Exploration, Environment, Analysis, 5,

723   247-253.

724   Scott, K. M., and Radford, N. W. (2007) Rutile compositions at the Big Bell Au deposit as a

725   guide for exploration. Geochemistry: Exploration, Environment, Analysis, 7, 353-361.

726   Smith, S. J., Stevens, R., Liu, S., Li, G., Navrotsky, A., Boerio-Goates, J., and Woodfield, B. F.

727   (2009) Heat capacities and thermodynamic functions of TiO2 anatase and rutile: Analysis of

728   phase stability. American Mineralogist, 94, 236-243.

729   Smyth, J. R. (2006) Hydrogen in high pressure silicate and oxide mineral structures. Reviews in

730   Mineralogy and Geochemistry, 62, 85-115.

731   Soffer, B. H. (1961) Studies of the optical and infrared absorption spectra of rutile single

732   crystals. The Journal of Chemical Physics, 35, 940-945.

733   Stepanov, A. S., and Hermann, J. (2013) Fractionation of Nb and Ta by biotite and phengite:

734   Implications for the "missing Nb paradox". Geology, 41, 303-306.

735   Swope, R. J., Smyth, J. R., and Larson, A. C. (1995) H in rutile-type compounds: I. Single-

736   crystal neutron and X-ray diffraction study of H in rutile. American Mineralogist, 80, 448-453.

737   Triebold, S., Luvizotto, G. L., Tolosana-Delgado, R., Zack, T., and von Eynatten, H. (2011)

738   Discrimination of TiO_2 polymorphs in sedimentary and metamorphic rocks. Contributions to

739   Mineralogy and Petrology, 161(4), 581-596.

740   Tompsett, G. A., Bowmaker, G. A., Cooney, R. P., Metson, J. B., Rodgers, K. A., and Seakins, J.

741   M. (1995) The Raman spectrum of brookite, TiO2 (PBCA, Z= 8). Journal of Raman

742   Spectroscopy, 26, 57-62.

743   Urban, A. J., Hoskins, B. F., and Grey, I. E. (1992) Characterization of V-Sb-W-bearing rutile

744   from the Hemlo gold deposit, Ontario. The Canadian Mineralogist, 30, 319-326.

745   Vikre, P.G. and John D.A., 2010 Chapter L. Hydrothermal alteration.in Descriptive Models for

746   Epithermal Gold-Silver Deposits, 125-142.

747   Vlassopoulos, D., Rossman, G. R., and Haggerty, S. E. (1993) Coupled substitution of H and

748   minor elements in rutile and the implications of high OH contents in Nb-and Cr-rich rutile from

749   the upper mantle. American Mineralogist, 78, 1181-1191.

750   Wright, D.M., Potter, E.G., and Comeau, J-S., (2015) Athabasca Basin Uranium Geochemistry

751   Database v.2; Geological Survey of Canada, Open File 7792, 1 .zip file. doi:10.4095/296461

752   Zack, T., and Kooijman, E. (2017) Petrology and geochronology of rutile. Reviews in

753   Mineralogy and Geochemistry, 83, 443-467.

754   Zeh, A., Cabral, A. R., Koglin, N., and Decker, M. (2018) Rutile alteration and authigenic

755   growth in metasandstones of the Moeda Formation, Minas Gerais, Brazil–A result of

756   Transamazonian fluid–rock interaction. Chemical Geology, 483, 397-409.

757   Zhang, H., and Banfield, J. F. (1999) New kinetic model for the nanocrystalline anatase-to-rutile

758   transformation revealing rate dependence on number of particles. American Mineralogist, 84,

759   528-535.

760 Zhang, H., and Banfield, J. F. (2000) Understanding polymorphic phase transformation behavior

761 during growth of nanocrystalline aggregates: insights from TiO2. The Journal of Physical

762 Chemistry B, 104, 3481-3487.

763

764 **List of Figure Captions**

765 **Figure 1.** a) A simplified sketch of Canada showing the locations of the Athabasca and Thelon

766 Basins, and map b. b) A regional map (modified from Jefferson et al. 2007) showing the

767 stratigraphic units of the eastern Athabasca Basin overlying the Rae and Hearne Provinces. The

768 location of the Wollaston Supergroup, the McArthur River deposit, P2 fault, and map c is also

769 shown. Stratigraphic units: RD = Read Formation, MFb = Bird Member, Manitou Falls

770 Formation, MFc = Collins Member, Manitou Falls Formation, MFd = Dunlop Member, Manitou

771 Falls Formation. c) A plan view map (modified from Adlakha et al. 2017 and updated according

772 to Bray et al. 2018) of the unconformity showing the P2 fault, mineralized zones of the

773 McArthur River deposit (from southwest to northeast: McA South 1, Zones 4-1, McA North 1,

774 Zone A, McA North 2, Zone B, McA North 3, and McA North 4), low-grade (P2 Main) and

775 unmineralized areas. Surface drillhole collar locations are indicated by a circle, and next to each

776 drillhole collar is a list of samples that were collect from that location (see Table 1). Samples

777 collected from drillholes collared in the underground mine are indicated with an arrow pointing

778 to its general location (i.e. mineralized zone)

779 **Figure 2.** Photographs of representative samples: a) brecciated graphitic (Gr) metapelite with

780 luecosome, b) brecciated quartzite, c) silicified (Qtz) graphitic metapelite overprinted by

781 desilicification and clay, d) silicificied metapelite cross-cut by blue veinlets of magnesio-foitite

782 (Mgf), e) graphitic metapelite pervasively altered to form magnesio-foitite, f) metapelite cross-

783 cut by pegmatite (right side), g) graphitic metapelite crosscut by a vein of uraninite (pointed with

784 an arrow) surrounded by alteration halo of hematite (Hem), and h) hematized, conglomeratic

785 quartz sandstone exhibiting silty layers that contain Ti-oxide. Scale bars = 1 cm

38

786   **Figure 3.** Representative Raman spectra for a) rutile and b) anatase.

787   **Figure 4.** Paragenetic sequence of rutile, anatase and co-existing phases, along the P2 fault, with

788   respect to the development of the Athabasca Basin. Dashed lines indicate uncertainty. OG =

789   quartz overgrowths; remob. = remobilized or secondary U-hydroxide

790   **Figure 5.** Photomicrographs (transmitted and reflected light) and SEM-BSE images of rutile. a)

791   Disseminated rutile (Type 1) with oxy-dravite (Dv) overprinted by magnesio-foitite with fine-

792   grained anatase (Ant). b) Rutile (Type 1) interlocked with anhedral oxy-dravite and surrounded

793   by lathlike graphite (Gr) and subhedral pyrite (Py). Graphite embays a chloritized mineral

794   interpreted to have been cordierite (Crd). c) Rutile (Type 1) with muscovite (Ms), zircon,

795   graphite, oxy-dravite, and quartz, overprinted by magnesio-foitite. Rutile needles (Type 3) along

796   the muscovite cleavage planes. d) Fractured rutile (Type 1) surrounded by fine-grained uranium

797   oxide (U), sudoite (Sud), and illite (Ilt). e) Rutile (Type 1) with muscovite and quartz containing

798   sillimanite (Sil) needles. An inset BSE image shows muscovite (Ms) with rutile and zircon.

799   Reddish color of muscovite is due to alteration forming fine-grained Fe-oxide. f) Fine-grained

800   blocky rutile (Type 2) with rounded inclusions of anatase (Ant^r) in an unknown coarse-grained

801   mineral (?) that is surrounded by sudoite and stringers of hematite (Hem). Sudoite with patchy,

802   and dendritic anatase (Ant^p, Ant^d, respectively) alter the mineral.

803   **Figure 6**. Photomicrographs (transmitted and reflected light) and SEM-BSE images of anatase.

804   a) Anatase (Ant) with dolomite (Dol) and coarse-grained hematite (Hem). An inset BSE image

805   showing zoned anatase with a core containing high W and Fe. b) A silty layer containing anatase

806   in quartz (Qz) sandstone. An inset BSE image showing anatase with late diagenetic illite (Ilt). c)

807   Anatase overprinting kaolin (Kln) and quartz overgrowths of detrital quartz. Quartz overgrowths

808   containing Sr-SO$_4$ rich APS minerals. Note black triangular grains (bottom right) are diamond

809   grit from polish paste trapped in clay. d) Lath-like anatase partially replaced by U-oxide. e)

810   Anatase with magnesio-foitite surrounding early rutile (Rt) and zircon (Zr). f) Coarse-grained

811   disseminated anatase.

812   **Figure 7.** Biplots of element abundances in rutile using EPMA data recalculated as atomic cation

813   percent: a) Ti and V, b) Nb and V, c) Nb and Fe, and d) Nb and V+Fe. Trendlines rooted at zero

814   are shown representing different substitution mechanisms.

815   **Figure 8.** Biplots of element abundances in anatase using EPMA data recalculated as atomic

816   cation percent: a) Ti and V, b) Nb and Fe, c) W and Fe, and d) Ti and Fe. Trendlines rooted at

817   zero are shown representing different substitution mechanisms.

818   **Figure 9.** Biplot diagrams showing LA-ICP-MS data for rutile and anatase: a) Ta vs. Nb/Ta, b)

819   Zr/Hf vs. Nb/Ta, and c) Th vs. U (in ppm), d) Fe/Nb vs V/Fe. The grey and orange fields in a and

820   b are for rutile in high-grade metasedimentary rocks from Luvizotto and Zack (2009) and Meyer

821   et al (2011), respectively. Lower Zr/Hf ratios reported by Meyer et al. (2011) shown in b are

822   explained by recrystallization by fluids during retrogression. The hydrothermal and mantle fields

823   shown in diagram b are modified from Pereira et al. (2019). Triangle markers indicate rutile that

824   occurs with oxy-dravite. Open diamonds represent anatase hosted in sandstone samples, whereas

825   filled diamonds represent anatase in basement metapelite. Color coding reflects sample position

826   along the P2 fault: green for unmineralized areas, blue for low-grade mineralized areas, purple

827   for Zone 1, red for Zone 2 and orange for Zone 4 (see Fig. 1C).

828

40

Tables

Table 1. Sample list and descriptions

DDH[a]	Sample	Depth (m)[b]	Lithology[c]	U mineralization[d]	Ti species[e]	Size (μm)	Crystal habit
MC349	MAC98	578	metapelite breccia/ gouge	low grade	Rt	20 - 100	Subhedral, fractured with corroded rims
					Ant	10 - 50	Blocky to dendritic fracture infill, rare euhedral crystal observed
MC349	MAC99	573	quartz+oxy-dravite graphitic metapelite breccia with intense magnesio-foitite alteration	low grade	Rt	50 - 150	Subhedral, fractured crystals
H3559	MAC201	-	quartz+oxy-dravite vein in graphitic metapelite	Z1	Rt	50 - 500	Subhedral to rounded, clean to corroded rims
H3576	MAC203	-	metapelite with luecosome	Z1	Rt	200 - 400	Subhedral, heavily fractured with corroded rims
H203	MAC152	-	graphitic metapelite	Z2	Rt	100 - 400	Subhedral, fractured with corroded rims
H203	MAC444	-	graphitic metapelite with 1 cm wide leucosome	Z2	Rt	50 - 300	Subhedral, fractured with corroded rims
H201	MAC70	-	graphitic metapelite breccia	Z2	Rt	20 - 100	Subhedral, fractured with corroded rims
H201	MAC441	-	graphitic metapelite with leucosome patches	Z2	Rt	50 - 200	Subhedral, fractured with corroded rims
H347	MAC79	-	yellow-clay altered quartzite breccia	Z2	Rt	50 – 500	Sub-anhedral, fractured
H493	MAC84	-	quartz+oxy-dravite graphitic metapelite breccia	Z2	Rt	50 - 200	Subhedral, fractured with corroded rims
H493	MAC86	-	graphitic metapelite with luecosomes breccia	Z2	Rt	50 - 150	Subhedral, fractured with corroded rims
H3380	MAC423	-	uraninite-hematite vein in graphitic metapelite	Z2	Ant	< 50	Blocky clusters to lath-like, coated in U oxide
H677	MAC420	-	metapelite with l0 cm wide pegmatite	Z4	Rt	50 - 400	Subhedral, fractured with corroded rims
MC410	MAC406	527.7	hematized, conglomeratic quartz sandstone	low grade	Ant	20 - 100	Blocky to anhedral patches
MC362	MAC127	602.3	graphitic metapelite breccia with luecosomes	unmin	Rt	40 - 250	Subhedral, fractured crystals
MC359	MAC426	581.6	local hematite-dolomite in graphitic metapelite	unmin	Ant	< 100	Euhedral to anhedral crystals with corroded rims
MC359	MAC430	494	hematized, conglomeratic quartz sandstone	unmin	Ant	< 50	Blocky to anhedral clusters
MC381	MAC436	603	quartz+oxy-dravite graphitic metapelite breccia with intense magnesio-foitite alteration	unmin	Rt	20 - 100	Euhedral crystals with corroded rims
					Ant	< 10	Blocky disseminations

a: diamond drill-hole; b: depth from surface; b: - = collared underground; c: pel = metapelite, peg = pegmatite, ss = sandstone, gr = graphitic, bx = breccia; d: unmin = no mineralization, low grade = sub-economic area, Z1-4 = Zone # ore body of the McArthur River deposit; e: Rt = Rutile, Ant = anatase

Table 2. Types of Ti-oxide occurrences

Mineral	Type	Mode of Occurrence	Spatially Associated minerals	Samples
<u>Rutile</u>[a]				
	Type 1	disseminated	oxy-dravite, graphite, pyrite, quartz, zircon	MAC84, MAC99, MAC127, MAC201, MAC420 MAC436
			quartz, graphite, pyrite, zircon,	MAC70, MAC86, MAC441, MAC444
			quartz	MAC98, MAC152, MAC203
			quartz, sillimanite, zircon, Fe-oxide altered muscovite	MAC79 (quartzite)
	Type 2	fg needles along cleavages of mica	chloritized muscovite	MAC70, MAC84, MAC86, MAC127, MAC423, MAC441, MAC444
	Type 3	fg blocky inclusions	altered amphibole, rounded anatase	MAC98
<u>Anatase</u>				
	SS-hosted	anhedral, patchy grains interstitial to detrital minerals	illite, kaolin, APS minerals, fg red hematite	MAC406, MAC430
	Basement-hosted	fg to cg anhedral disseminations	magnesio-foitite, sudoite, illite, LREE-rich APS minerals, late U-oxide	MAC98, MAC436
		lath-like mica pseudomorphs	U-oxide, magnesio-foitite, sudoite, illite, LREE-rich APS minerals, late U-oxide	MAC423
		rounded inclusions	Type 2 rutile	MAC98
		dendritic veinlets and anhedral patchy grains	Sudoite, fg red hematite, LREE-rich APS, late U-oxide	MAC98
		euhedral cg crystals	dolomite, cg black hematite	MAC426

cg = coarse-grained, fg = fine-grained; Notes: a: All rutile occurs in basement rocks.

842

Table 3. Average composition of rutile in wt.% (EPMA) and ppm (LA-ICP-MS) with standard deviation (1σ)

Sample	MAC152		MAC201		MAC70		MAC86		MAC420	
wt.%; n =	48/11		33/9		19/8		14/6		18/9	
	x̄	±	x̄	±	x̄	±	x̄	±	x̄	±
Cr	0.15	0.10	0.03	0.01	0.13	0.02	0.11	0.04	0.13	0.03
Nb	0.32	0.05	0.33	0.09	0.33	0.10	0.29	0.09	0.30	0.13
Zr	0.07	0.02	0.08	0.03	0.06	0.02	0.06	0.02	0.07	0.03
Ta	<0.01		<0.01		<0.01		<0.01		<0.01	
Ti	59.32	0.19	59.51	0.22	59.46	0.25	59.32	0.17	59.53	0.27
W	0.08	0.03	0.21	0.05	0.05	0.03	0.06	0.03	0.07	0.05
V	0.23	0.12	0.28	0.03	0.30	0.03	0.58	0.13	0.30	0.10
Fe	0.11	0.04	0.16	0.03	0.07	0.03	0.05	0.02	0.08	0.04
O	40.07	0.09	40.22	0.11	40.19	0.14	40.19	0.1	40.21	0.06
Total	100.41	0.20	100.86	0.26	100.66	0.39	100.75	0.25	100.75	0.14
ppm; n =	12/9		14/11		6/6		9/8		10/10	
Al	264	128	183	76.8	1780	2380	720	933	1740	4490
Si	205	391	114	210	3610	3847	763	957	4980	6910
Ca	3.17	7.09	25.9	27.5	44.7	31.9	12.6	19.6	23.4	33.4
Sc	211	126.0	102	5.68	93.2	9.29	73.2	8.03	93.9	19.0
V	3540	1210	3890	222	4610	777	6620	1520	4360	873
Cr	1660	837	407	39.1	1560	344	1090	304	1390	228
Mn	1.66	1.52	0.64	0.86	3.35	1.75	1.51	1.50	1.47	1.53
Fe	830	370	1410	240	837	445	437	220	883	454
Co	0.110	0.144	0.008	0.013	0.657	0.824	0.176	0.273	13.2	29.7
Ni	0.236	0.351	0.371	0.160	1.44	1.61	1.01	1.10	11.5	29.0
Cu	3.47	2.81	1.50	0.354	4.81	4.10	1.53	0.29	1.15	0.572
Zn	4.59	1.56	6.79	1.50	6.13	2.79	4.99	1.40	3.69	0.63
Ga	0.482	0.184	0.696	0.586	1.29	1.50	0.536	0.460	1.07	2.16
Ge	1.76	1.03	0.729	0.683	0.333	0.553	0.833	0.512	1.03	0.934
Se	14.7	23.5	36.9	50.7	14.5	15.9	14.4	30.1	5.00	15.0
Y	0.312	0.518	0.077	0.092	1.47	1.69	0.387	0.280	0.391	0.610
Zr	743	136	867	140	656	126	616	96.9	726	207
Nb	2970	302	3080	615	3060	939	3010	442	3460	1060
Mo	7.91	3.39	7.05	3.22	6.51	5.67	9.42	6.55	9.43	3.94
Sn	212	31.8	93.1	12.7	188	13.1	206	11.3	219	21.3
Sb	1.17	0.544	0.246	0.303	1.34	0.447	1.41	0.263	1.01	0.325
Hf	45.5	6.12	47.5	6.12	36.9	4.84	35.1	3.15	42.2	13.3
Ta	290	65.2	230	60.4	176	48.9	177	86.6	330	133
W	963	76.2	2540	295	684	207	852	103	992	450
Pb	0.257	0.467	0.070	0.053	2.47	2.82	0.836	0.782	0.262	0.277
Th	0.742	1.47	0.237	0.426	10.7	15.6	3.37	2.63	3.68	6.01
U	69.6	10.4	30.7	7.72	36.5	6.20	75.0	10.4	39.0	7.08

Note: EPMA data of Al, Si, Th, U, Mn, Mo were close to or below detection limits. Numbers below sample numbers indicate: number of data points/ number of grains. All data is of Type 1 disseminated rutile, except for MAC98T3 which is of Type 3 rutile inclusions.

843

Table 3. continued

Sample	MAC441		MAC84		MAC127		MAC203		MAC79	
wt.%; n =	21/6		27/10		27/12		(6/2)		8/4	
	x̄	±	x̄	±	x̄	±	x̄	±	x̄	±
Cr	0.12	0.02	0.07	0.03	0.13	0.03	0.03	0.03	0.13	0.02
Nb	0.41	0.10	0.26	0.02	0.22	0.12	0.69	0.11	0.92	0.11
Zr	0.08	0.02	0.07	0.02	0.07	0.02	0.12	0.02	0.08	0.03
Ta	<0.01		<0.01		<0.01		0.05	0.02	0.06	0.07
Ti	59.34	0.57	58.77	0.32	59.39	0.25	59.00	0.20	58.69	0.22
W	0.04	0.02	0.39	0.04	0.02	0.02	0.17	0.04	0.08	0.02
V	0.18	0.02	0.99	0.23	0.58	0.11	0.10	0.05	0.10	0.05
Fe	0.15	0.04	0.05	0.02	0.06	0.02	0.30	0.07	0.38	0.07
O	40.16	0.25	40.03	0.13	40.18	0.12	40.05	0.09	39.99	0.11
Total	100.59	0.63	100.67	0.29	100.70	0.30	100.55	0.20	100.48	0.28
ppm; n =	10/10		8/7		10/9		9/6		6/5	
Al	264	136	81.3	76.1	106	61	497	141	265	83
Si	124	249	66.3	175	219	318	382	419	3270	5450
Ca	38.0	40.0	16.0	27.8	26.8	32.7	13.3	18.0	8.33	18.6
Sc	94.1	13.0	97.2	27.0	92.9	15.4	774	185	94.9	4.10
V	2650	306	12100	2540	6370	1240	1840	362	2170	333
Cr	1260	209	904	277	1220	105	258	127	1210	206
Mn	0.66	1.17	2.63	6.91	0.88	0.82	1.87	1.13	0.87	0.90
Fe	1560	480	197	129	410	53	2780	580	3270	954
Co	0.001	0.004	0.029	0.048	0.008	0.010	0.001	0.004	0.026	0.027
Ni	0.098	0.126	0.115	0.115	0.216	0.166	0.086	0.169	0.032	0.038
Cu	0.791	0.229	1.50	0.554	0.956	0.259	0.894	0.143	1.84	0.755
Zn	3.03	1.67	4.94	1.07	3.35	1.38	3.26	0.92	5.83	2.67
Ga	0.920	0.655	0.175	0.226	0.465	0.425	2.84	0.595	0.815	0.277
Ge	0.650	0.879	1.41	1.06	0.960	0.880	0.489	0.614	0.433	0.556
Se	25.5	22.9	2.00	5.29	6.70	11.1	16.2	15.4	15.8	16.5
Y	0.026	0.006	0.166	0.248	1.65	4.84	0.106	0.161	3.58	7.79
Zr	816	75.9	623	63.5	699	91.1	1010	53.2	638	130
Nb	5410	2660	2580	248	2060	606	7770	1140	7860	1870
Mo	3.84	0.725	5.45	4.86	10.7	7.13	14.1	4.00	19.1	11.5
Sn	162	13.1	389	27.1	181	8.89	238	80.0	204	17.2
Sb	0.305	0.229	0.765	0.353	1.15	0.258	0.573	0.328	0.433	0.253
Hf	43.7	3.56	36.8	3.12	35.5	3.37	52.5	2.57	33.3	7.31
Ta	458	297	225	36.7	147	90.9	711	173	721	321
W	514	118	4440	226	219	34.0	1920	422	1040	229
Pb	0.023	0.026	0.299	0.466	0.594	1.68	0.031	0.059	0.262	0.487
Th	0.00	0.00	1.72	3.02	2.34	7.02	0.148	0.418	0.517	1.15
U	16.5	1.22	92.7	9.67	77.5	16.5	23.5	1.79	51.2	9.30

844

845

Table 3. continued

Sample	MAC99		MAC444		MAC436		MAC98		MAC98-T2	
wt.%; n =	18/10		12/5		12/7		13/5		5/5	
	x̄	±	x̄	±	x̄	±	x̄	±	x̄	±
Cr	0.02	0.01	0.18	0.03	0.10	0.02	0.12	0.05	0.14	0.02
Nb	0.77	0.08	0.25	0.07	0.24	0.05	2.33	0.39	2.23	0.15
Zr	0.07	0.01	0.07	0.02	0.07	0.02	0.07	0.02	0.02	0.02
Ta	<0.01		<0.01		<0.01		0.14	0.11	0.02	0.03
Ti	59.04	0.17	59.18	0.16	59.21	0.24	56.54	0.70	56.59	0.61
W	0.05	0.03	0.06	0.03	0.18	0.03	0.35	0.15	0.07	0.05
V	0.13	0.02	0.64	0.15	0.49	0.06	0.84	0.12	1.10	0.10
Fe	0.37	0.07	0.04	0.02	0.04	0.01	0.61	0.17	0.33	0.21
O	40.1	0.09	40.1	0.03	40.06	0.17	39.71	0.14	39.65	0.27
Total	100.60	0.22	100.56	0.11	100.46	0.46	100.84	0.21	100.32	0.68
ppm; n =	10/8		9/9		10/10		3/3			
Al	327	119	76.8	150	80.9	34.8	628	173		
Si	350	346	602	1039	168	339	877	996		
Ca	19.1	31.3	29.9	32.6	5.7	8.61	12.3	10.2		
Sc	90.8	9.04	95.4	18.2	94.8	16.5	142	17.6		
V	2280	193	6820	1330	5760	1090	10200	996		
Cr	322	26.1	1490	465	1110	232	1370	367		
Mn	0.97	1.55	1.52	1.71	0.42	0.77	1.57	1.14		
Fe	2980	521	235	78.2	352	158	6010	997		
Co	0.008	0.023	0.035	0.048	0.008	0.012	0.015	0.015		
Ni	0.124	0.187	0.187	0.197	0.220	0.166	0.337	0.104		
Cu	1.31	0.164	0.898	0.207	1.19	0.231	1.31	0.141		
Zn	4.84	1.17	3.31	1.27	3.89	0.98	4.83	1.32		
Ga	1.10	0.389	0.084	0.143	0.335	0.425	2.22	0.684		
Ge	0.980	0.812	0.622	0.739	1.01	0.692	0.967	0.544		
Se	20.7	25.8	7.89	11.6	19.0	24.3	19.0	13.7		
Y	0.057	0.028	0.054	0.074	0.482	1.34	0.057	0.016		
Zr	679	51.7	718	130	719	87.0	621	149		
Nb	7080	1530	2640	497	3140	1180	24200	721		
Mo	5.22	2.87	3.59	2.79	0.771	0.654	11.2	6.60		
Sn	58.5	5.10	147	12.8	215	35.1	297	14.0		
Sb	0.129	0.132	0.579	0.358	0.608	0.271	0.180	0.083		
Hf	37.6	2.87	36.6	5.83	37.8	4.83	35.2	6.16		
Ta	531	142	365	149	349	183	2710	251		
W	633	59.8	495	190	1490	402	4290	907		
Pb	0.070	0.127	0.021	0.025	0.055	0.065	0.020	0.029		
Th	0.033	0.096	0.039	0.110	0.123	0.369	0.000	0.000		
U	10.9	0.747	29.2	9.41	41.0	10.4	24.7	3.82		

846

847

67

Table 4. Averaged composition of anatase in elemental wt.% (EPMA) and ppm (LA-ICP-MS) with standard deviation (1σ).

Sample	MAC426		MAC436		MAC98-inc		MAC98-patchy		MAC430		MAC406	
wt.%; n =	11/6		3/2		(2/1)		(8/6)		11/6		11/8	
	x̄	±	x̄	±	x̄	±	x̄	±	x̄	±	x̄	±
Cr	0.05	0.06	<0.01		<0.01		<0.02		<0.01		<0.01	
Nb	0.18	0.02	0.10	0.07	0.11	0.02	0.06	0.04	0.25	0.10	0.23	0.02
Zr	0.19	0.09	<0.02		0.02	0.01	<0.01		0.06	0.04	0.02	0.02
Ti	59.48	0.77	60.03	0.30	60.13	0.11	59.98	0.15	59.40	0.30	59.45	0.28
W	0.28	0.54	0.02	0.02	<0.01		<0.01		<0.01		<0.01	
V	<0.01		<0.01		<0.01		0.11	0.12	<0.01		<0.01	
Fe	0.31	0.24	0.08	0.01	0.21	0.03	0.18	0.13	0.42	0.15	0.40	0.16
O	40.12	0.27	40.26	0.17	40.35	0.05	40.29	0.08	40.05	0.08	40.09	0.11
Total	100.62	0.32	100.57	0.48	100.78	0.16	100.78	0.16	100.27	0.15	100.32	0.24
ppm; n =	7/7		1/1				1/1		3/3		5/5	
Al	282	608	5850				500		3020	3470	3610	2530
Si	1430	2170	4780				0		17600	12500	4610	3240
Ca	1770	3310	2.00				26		168	80.2	225	62.1
Sc	30.3	21.4	2.29				42.6		101	58.3	64.8	9.62
V	85.5	55.8	12.9				116.9		86.5	50.1	77.8	11.3
Cr	401	287	2.00				259		20.3	9.81	192	22.6
Mn	15.4	28.3	0.000				0.6		5.90	4.34	7.36	1.63
Fe	1480	318	505				1562		4950	1610	5970	941
Co	0.266	0.568	0.035				0		0.016	0.005	0.011	0.012
Ni	0.627	1.33	1.97				0.37		0.073	0.104	0.306	0.169
Cu	1.04	0.405	1.58				1.89		1.06	0.269	2.342	0.442
Zn	3.93	0.928	3.40				4.7		5.67	1.87	4.92	1.21
Ga	0.082	0.183	1.72				0.22		0.977	0.803	1.50	0.606
Ge	0.614	0.541	2.00				1.6		0.467	0.525	0.260	0.520
Se	9.29	15.2	0.000				0		31.7	44.8	18.8	23.0
Y	0.742	0.451	0.111				0.112		4.30	3.28	7.81	1.45
Zr	2610	671	11.4				169.9		559	73.8	463	77.8
Nb	1870	70.7	1160				836		4910	4060	2190	175
Mo	0.077	0.114	0.000				3.1		2.07	0.611	6.57	1.59
Sn	95.8	21.2	0.550				0.39		70.4	96.0	3.10	0.541
Sb	0.026	0.127	0.000				0		3.15	1.60	3.77	0.755
Hf	140	15.4	0.760				2.81		22.9	8.80	14.5	3.09
Ta	158	11.7	35.2				58.7		470	517	119	48.2
W	585	337	51.9				93.8		93.0	36.8	27.0	1.82
Pb	4.02	2.76	0.210				0.82		12.9	8.01	27.2	4.04
Th	30.5	22.2	0.380				3.61		12.0	9.82	37.0	7.25
U	9.74	7.37	1.49				115		71.7	44.8	149	32.0

Note: EPMA of Al, Si, Mg, Mn, Mo, Sn, Ta, Th, U <0.02 wt.%
Number in parentheses below sample numbers indicate: (number of data points/ number of grains) analysed. MAC98inc = rounded inclusions; MAC98-patchy = patchy replacement
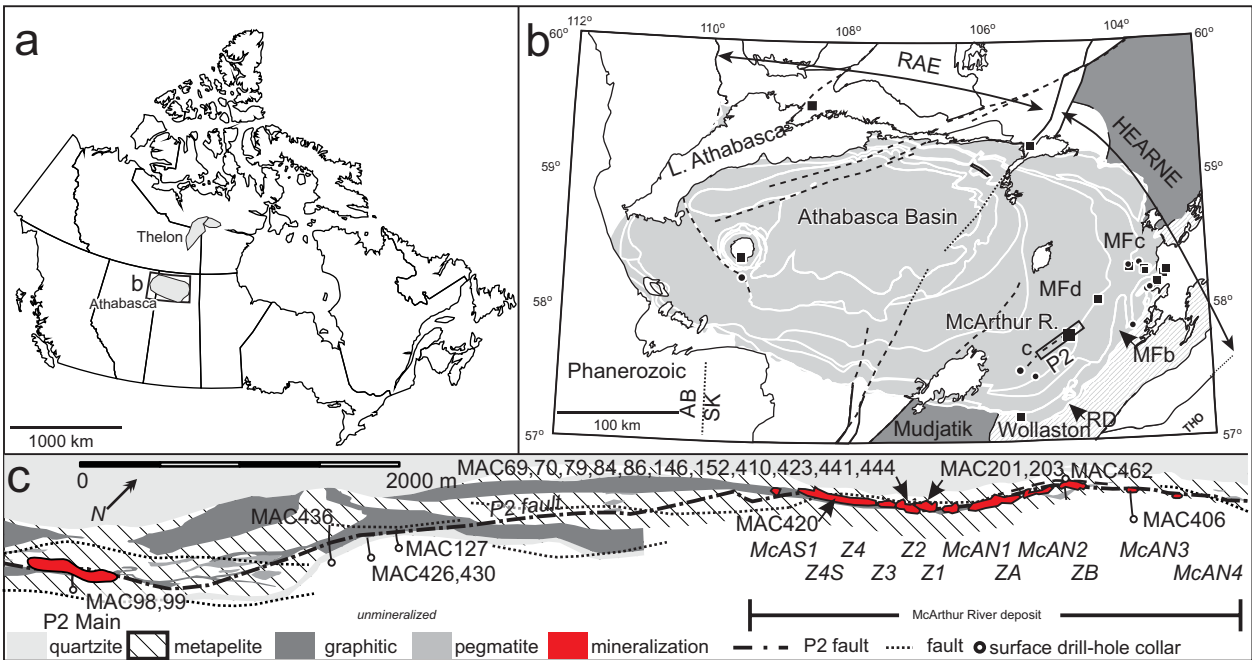
Figure 1

a *MAC86 graphitic metapelite breccia*
Gr

b *MAC79 quartzite breccia*

c *MAC152 graphitic metapelite*
Qtz

d *MAC99 graphitic metapelite breccia*
Mgf

e *MAC436 graphitic metapelite breccia*
Mgf

f *MAC420 pegmatite in metapelite*

g *MAC423 U-vein in graphitic metapelite*
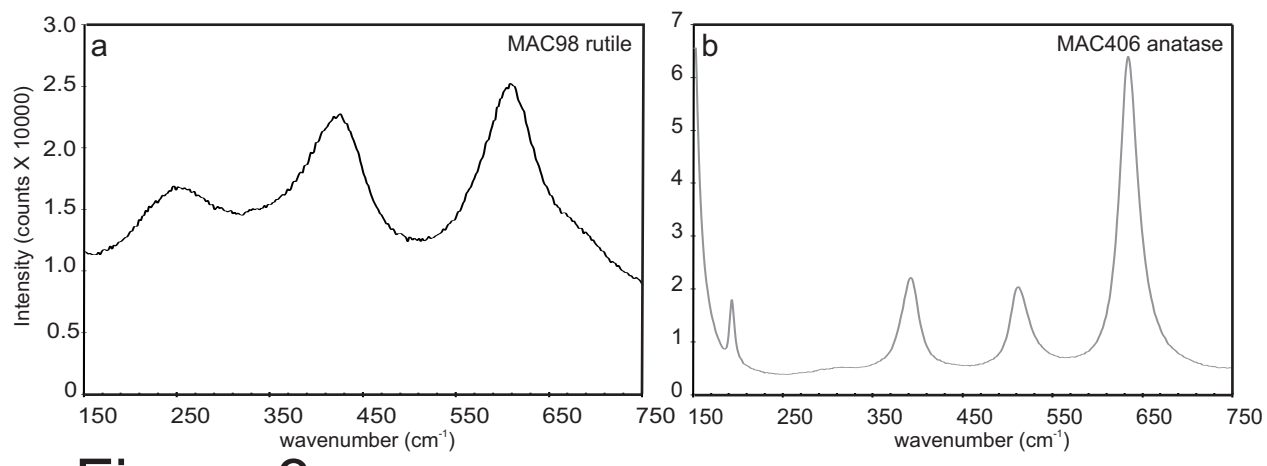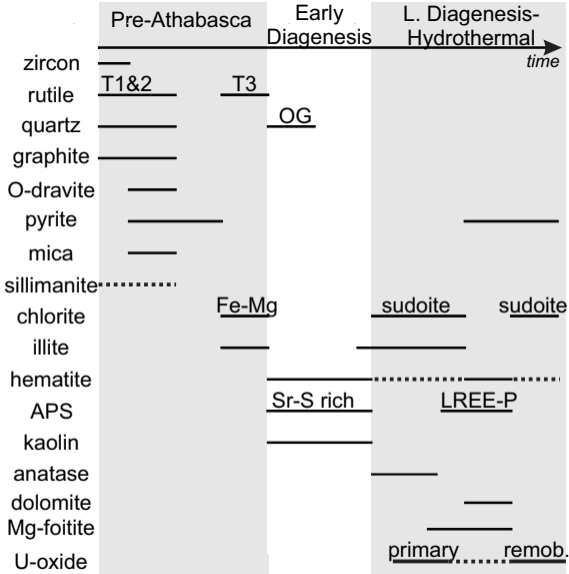U

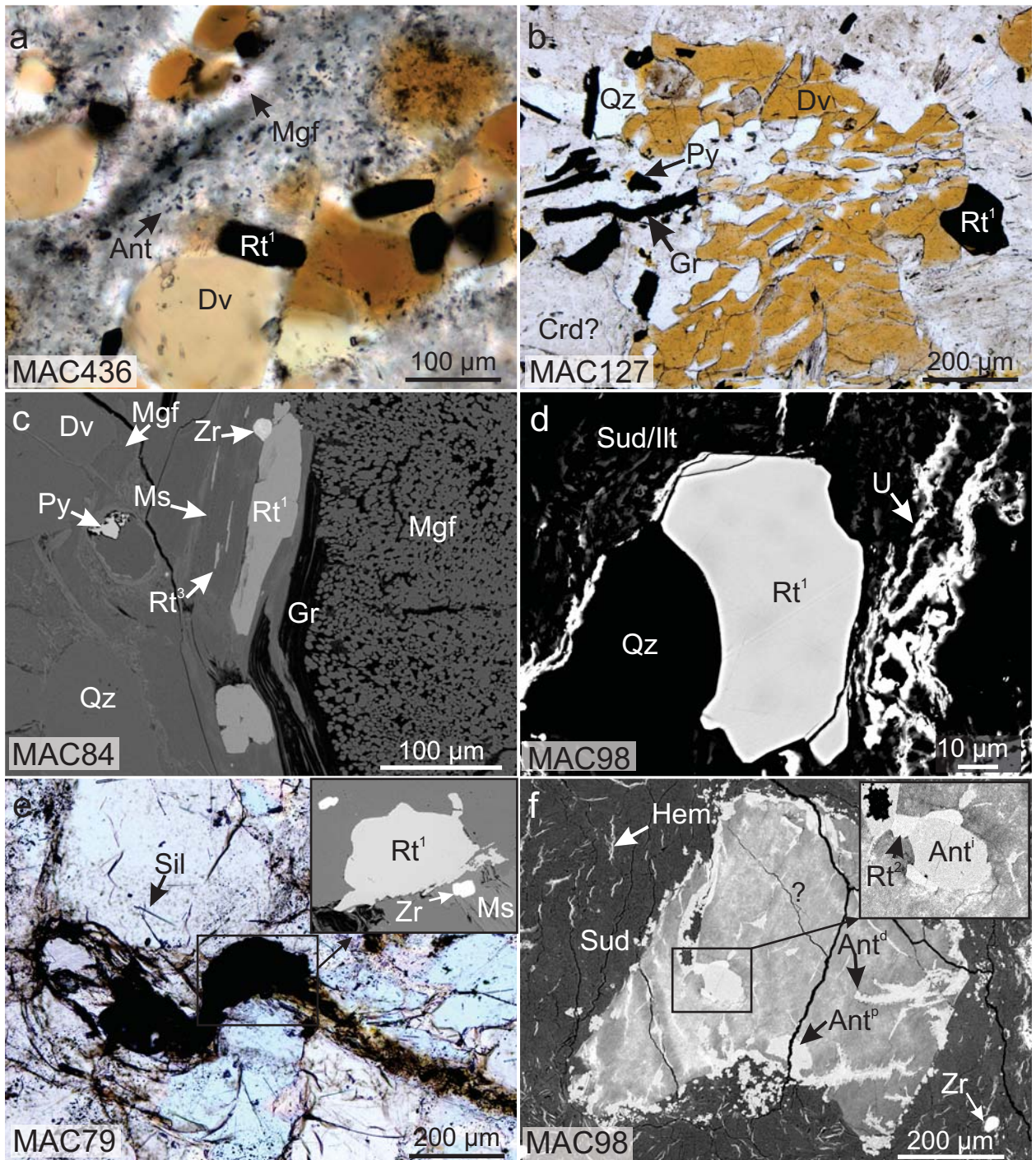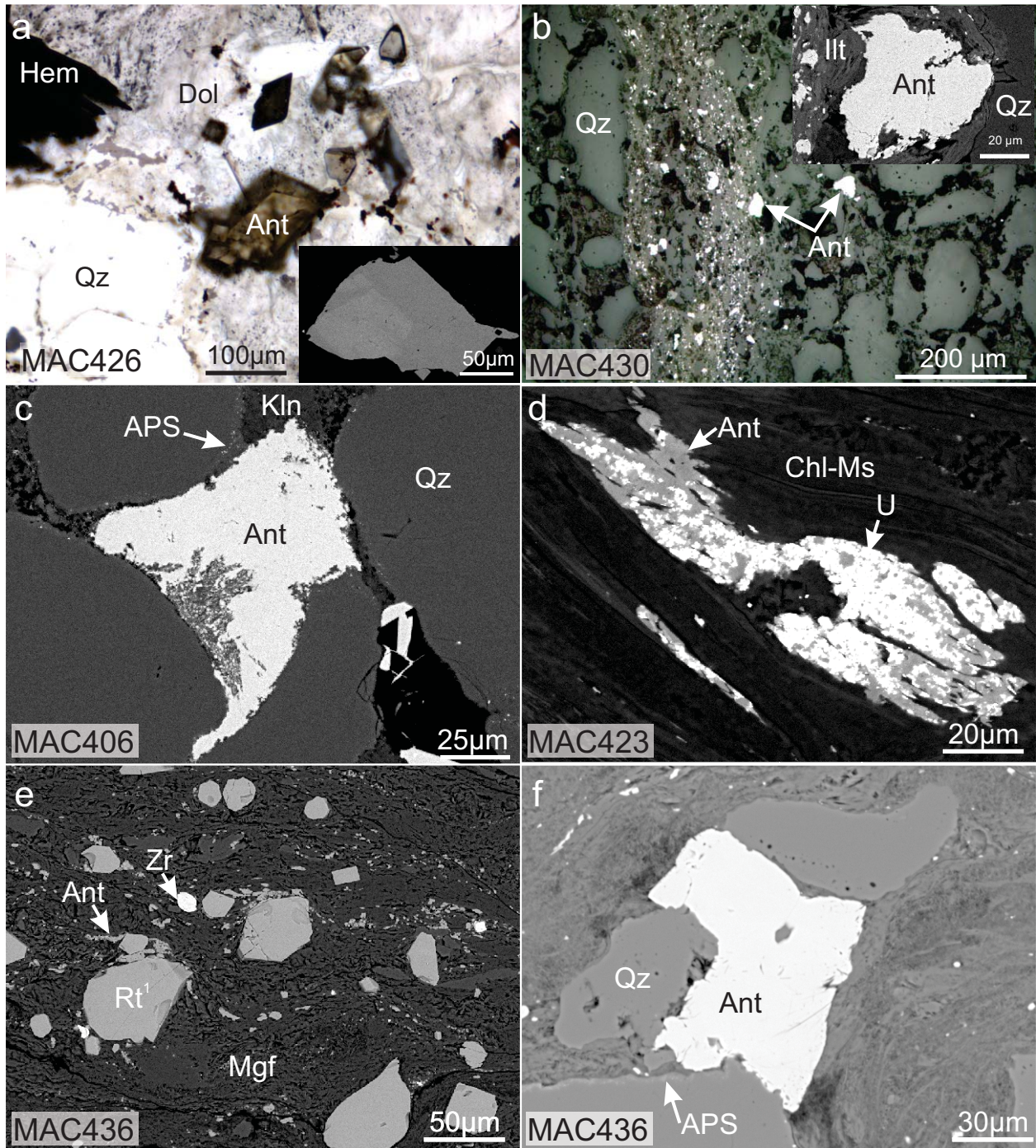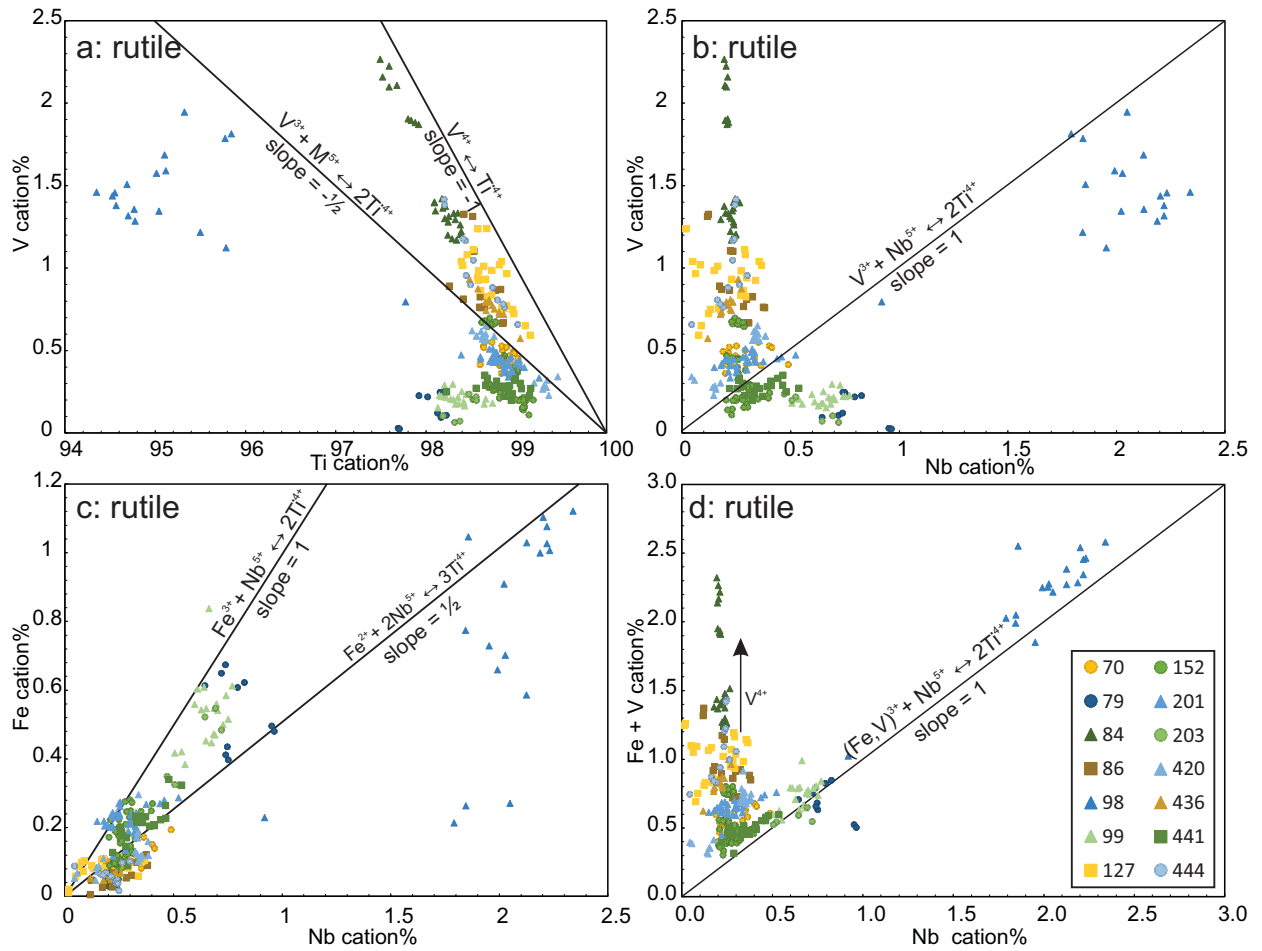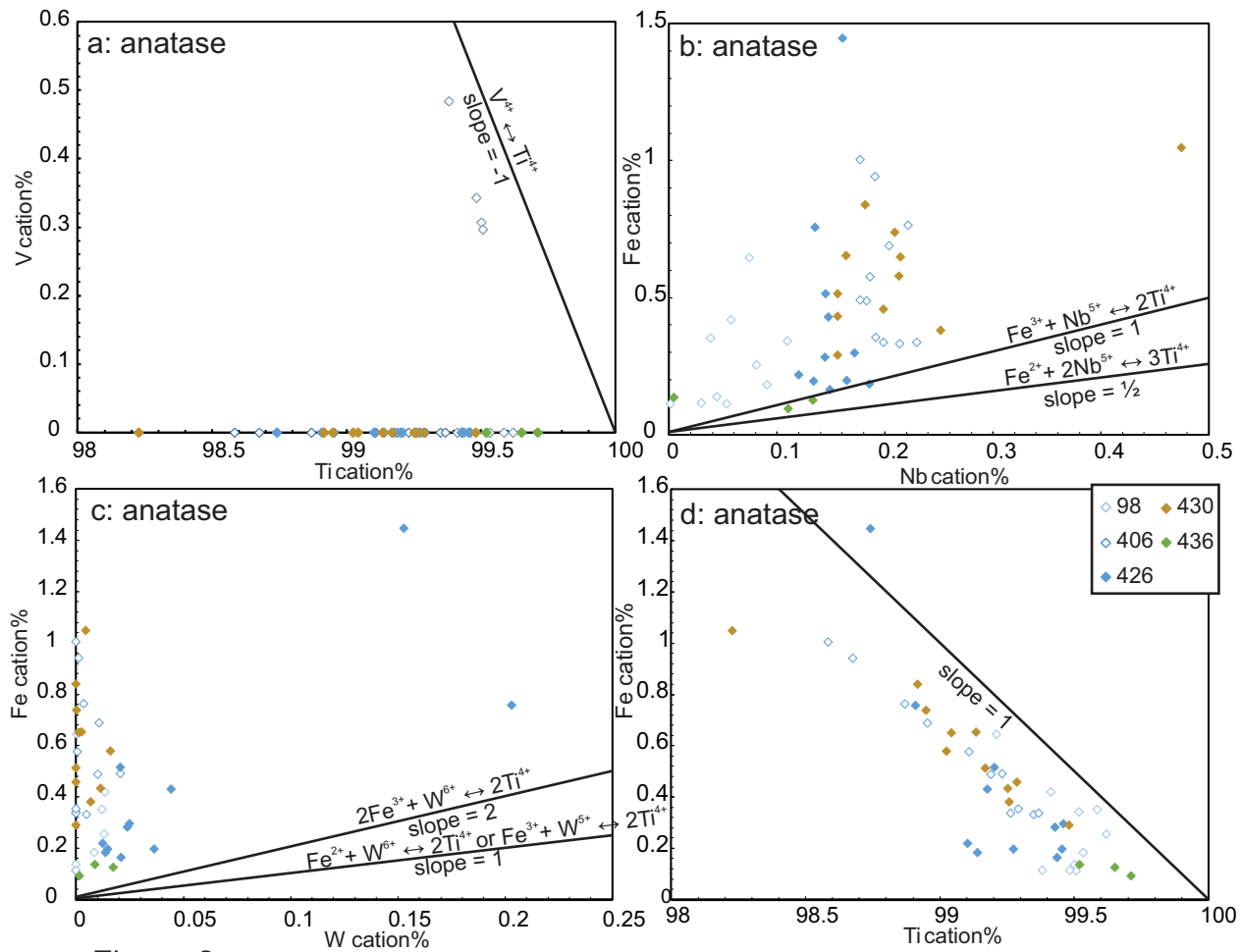h *MAC406 conglomeratic quartz sandstone*
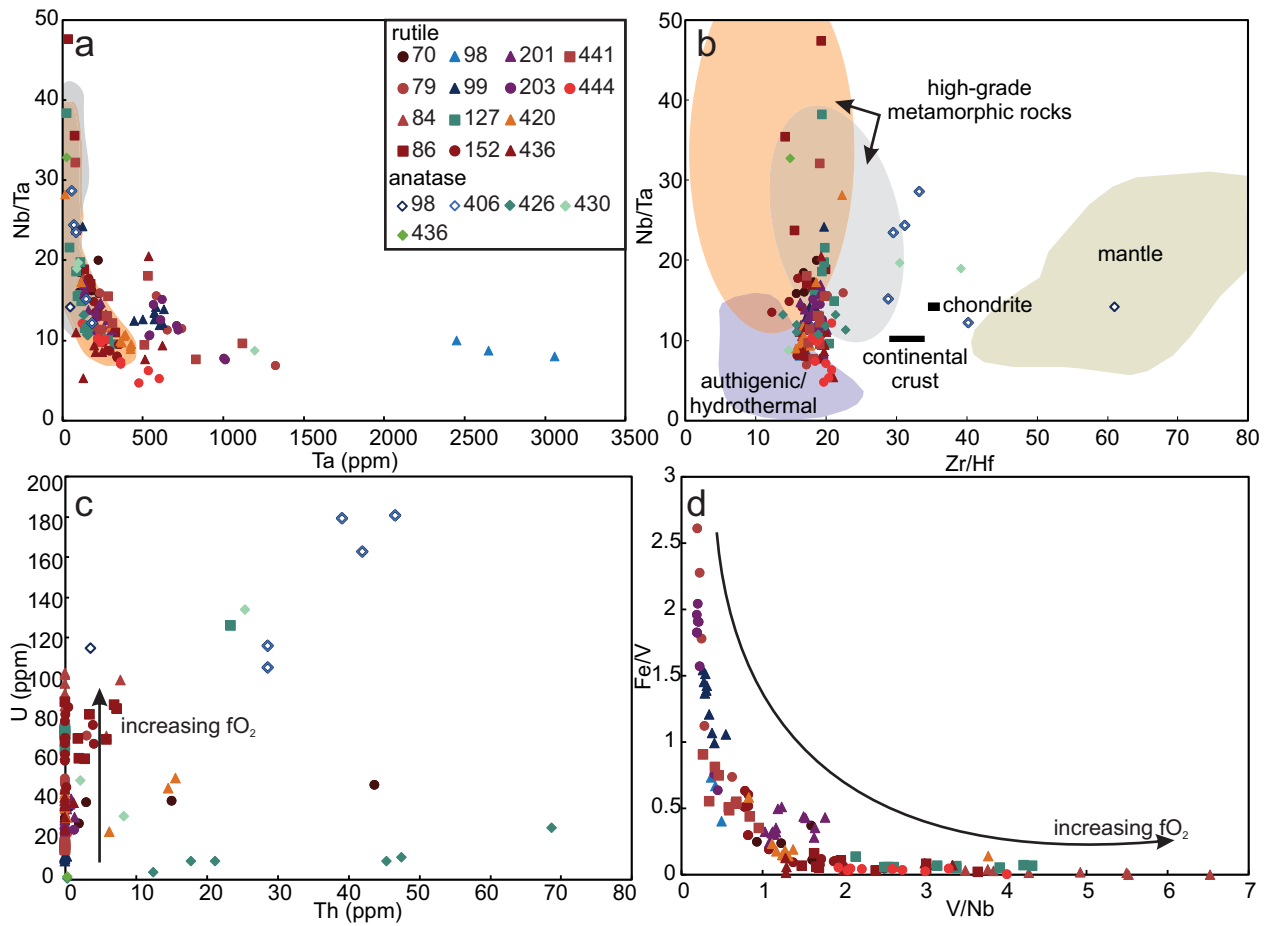silty layers

Figure 2

Figure 3

Figure 4

Figure 5

Figure 6

Figure 7

Figure 8

Figure 9